The anelasticity of zinc and its implications for the Earth's inner core *

Simon A. Hunt[1], Andrew M. Walker[2], Oliver T. Lord[3], Stephen Stackhouse[2], Lewis Schardong[1,4], Lora S. Armstrong[5], Andrew J. Parsons[2,6], Geoffrey E. Lloyd[2], Matthew L. Whitaker[7]

[1]Department of Earth Sciences, University College, London, Gower Street, London, WC1E 6BT. UK

[2]School of Earth and Environment, University of Leeds, Leeds LS2 9JT, UK

[3]School of Earth Sciences, University of Bristol, Wills Memorial Building, Queen‘s Road, Bristol BS8 1RJ, UK

[4]now at: Dept. of Geosciences, Raymond & Beverly Sackler Faculty of Exact Sciences, Tel Aviv University, Israel

[5]Department of Earth and Environmental Sciences, University of Minnesota, 150 Tate Hall, Minneapolis, Minnesota 55455, U.S.A.

[6]now at: Department of Earth Sciences, University of Oxford, South Parks Road, Oxford, OX1 3AN, UK

[7]Mineral Physics Institute, Stony Brook University, New York, USA

Key Points:

- The inner-core analogue zinc shows anelastic softening at seismic frequencies and high temperatures
- Substantial anelastic softening is possible even in the absence of a fluid or significant impurities
- Anelasticity must be accounted for when interpreting the inner core's seismic velocity and structure

---

***This is a non-peer reviewed preprint submitted to EarthArXiv**. The manuscript has been submitted for consideration for publication and peer review by *Journal of Geophysical Research: Solid Earth*. If accepted for publication, further details and a link to the post-review version will be provided on EarthArXiv.

Corresponding author: Simon A. Hunt, `simon.hunt@ucl.ac.uk`

Abstract

The Earth's inner core exhibits significant anisotropy in both seismic velocity and attenuation as well as hemispherical and depth variations. These observations point to an inner core that is both complex and dynamic. However, interpretation of these observations without knowledge of the attenuation processes active in the inner-core is difficult. To address this we have used zinc, as a low-pressure analogue of the hexagonal close pack (*hcp*) structured iron that forms the inner core, to provide first-order constraints on the anelasticity of *hcp* metals at seismic frequencies and high temperatures. A D-DIA apparatus was combined with X-radiography were utilised to measure the anelastic response of zinc up to a homologous temperature (T/T_m) of ≈ 0.8. To analyse the data we developed an improved image processing method that reduces systemtic errors and gives up to 3 orders of magnitude improvement in strain measurement precision. Using this algorithm, in the frequency range 0.1 to 0.003Hz, significant dissipation and softening of zinc's Young's modulus is observed. The softening occurs in the absence of significant impurities or a fluid phase and appears to be caused by, or related to, recrystallisaton of the samples in response to the stress. The recrystallisation results in a steady-state grain-size and low dislocation density. The predicted reduction in shear wave speed is 2-3 times greater than that of for compressional waves, which is consistent with anelasticity playing a significant role in the seismic velocity of the inner core. Therefore anelastic effects in *hcp* iron must be considered in the interpretation of inner-core.

1 Introduction

The solid inner core is the most remote and inaccessible part of our planet but its structure and composition may provide a key record needed to untangle the geological history of the surface environment. Information encoded in the inner core during its solidification could reveal the timing and nature of the onset of Earth's protective magnetic field generated by convection in the liquid outer core or even of changes in the way the mantle convects and drives surface dynamics [e.g. *Aubert et al.*, 2008]. Key to developing our understanding of the inner core is our ability to use seismic observations to constrain its structure on all scales. Seismic wave velocities are strongly sensitive to the atomic scale crystal structure, temperature and composition of the media through which they travel. They are also sensitive to the larger grain-scale microstructure, which reflects the deformation and crystallization history of the medium and can be probed by seismic studies of elastic anisotropy (variation of wave velocity with direction) and attenuation (reduction in wave amplitude with distance).

The anisotropy of the inner core's seismic velocity is well established [*Sumita and Bergman*, 2015; *Deuss*, 2014; *Woodhouse et al.*, 1986] with the velocity in the polar direction faster than equatorial directions [e.g. *Morelli et al.*, 1986]. The top 50-275 kms of the inner core are isotropic [*Shearer*, 1994; *Irving and Deuss*, 2011] but there are differences between the Eastern and Western hemispheres *Niu and Wen* [2001]. The velocity anisotropy increases with depth into the inner core [*Lythgoe et al.*, 2014].

Attenuation is quantified and reported as the inverse of the seismic quality factor. The seismic quality factor, Q, is equal to the fraction of energy absorbed per oscillation of a wave [*Stein and Wysession*, 2013; *Romanowicz and Mitchell*, 2015]. An undamped oscillator with no attenuation or energy loss has $Q = \infty$ ($Q^{-1} = 0$). Using body waves, Q has been estimated for the inner-core to be $\sim$ 200 just below the inner-core boundary increasing to 1000–2000 at the center of the Earth [*Doornbos*, 1974]. Significant regional variation in Q has been found to exist by *Pejić et al.* [2019] and *Li and Cormier* [2002], who also found a global mean $Q_{1\,\mathrm{Hz}} \sim 300$. Attenuation is also anisotropic [e.g. *Yu and Wen*, 2006], with hemispherical [*Cao and Romanowicz*, 2004] and depth variations [*Suda and Fukao*, 1990] in attenuation observed. Using normal modes, *Mäkinen et al.* [2014] showed that attenuation in the inner core is directionally dependent with the North-South direction being both seismically faster and more attenuating than radial directions.

Attenuation is, in turn, governed by the deformation modes of solids which are dependent on the time scale and magnitude of stress as well as the temperature, pressure and microstructure. On the shortest time scales, at temperatures below the melting point, small stresses result in elastic strains where stored energy is immediately returned once the stress is removed. On the longest time scales and typically at higher temperature, stress can cause the motion of defects leading to irrecoverable plastic deformation; for the inner core this is likely to be mediated by diffusion creep [*Orman*, 2004; *Sumita and Bergman*, 2015]. Between these extremes, stress applied at seismic frequencies leads to strain by the realignment of crystal defects (e.g. dislocations, twins, etc.). When the stress is removed the strain disappears after a delay time that is characteristic of the deformation mechanism. This anelasticity leads to frequency dependent moduli and loss of energy from the mechanical system. These processes are seismically observed and known to seismologists as dispersion and intrinsic attenuation. They link seismology and the nature of the imperfections within crystals that are the inevitable result of deformation or growth. Therefore, seismic observation of dispersion and attenuation in the inner core provides key information on its growth and dynamics. Crucial to its interpretation though is determining the dissipative process that causes it.

Attenuation mechanisms that have been proposed for the inner-core include partial melt [*Singh*, 2000; *Fearn et al.*, 1981], grain boundary relaxation, and dislocation related relaxations [*Jackson et al.*, 2000]. *Mäkinen et al.* [2014] preferred Zenner relaxation to explain inner-core attenuation; in this mechanism Fe atoms switch positions with vacancies and/or solute atoms as a result of the stress imparted by the passing seismic wave. All of these have been observed in geological samples or metals, albeit at less extreme conditions.

The possible attenuation modes are controlled by the phase through which the waves pass. It is widely, although not universally, accepted that iron in the inner core adopts the hexagonal close pack (*hcp*) structure stable above 10 GPa [e.g. *Tateno et al.*, 2010], albeit diluted by a light element [*Bazhanova et al.*, 2017; *Fei et al.*, 2016; *Antonangeli et al.*, 2018, 2010; *Fiquet*, 2001; *Mao et al.*, 2012; *Caracas*, 2015; *Sakamaki et al.*, 2016; *Tagawa et al.*, 2016; *Tateno et al.*, 2012, 2015; *Prescher et al.*, 2015; *Li et al.*, 2018]. Based on theoretical calculations of viscosity *Belonoshko et al.* [2019] argued that anelasticity of the inner core is incompatible with that observed for *hcp* metals, and so iron adopting *bcc* structure in the inner core. In general, experimental and computational studies investigating inner core properties and chemistry, implicitly assume negligible anelastic attenuation and no modification to the seismic wave speed.

The experimental data needed to distinguish between the proposed mechanisms and interpret the seismological observations does not exist because of the extreme conditions of both the inner core and under which *hcp* iron is stable. The most recent study of the anelasticity of iron [*Jackson et al.*, 2000] is almost two decades old and is limited to low pressure where iron adopts the body centred cubic (*bcc*) or face centred cubic (fcc) structure. Atmospheric pressure measurements of anelasticity of *hcp*-metals have generally been performed at much higher frequencies than seismic waves [e.g. *Wuttig et al.*, 1981; *Aning et al.*, 1982; *Takahashi*, 1952]. *Roberts and Brown* [1962] measured the anelasticity of zinc with periods between 10 and 100 seconds and attributed the anelasticity to dislocation motion. No further work has been done experimentally since and there are no measurements of anelasticity in *hcp*-metals at elevated pressure and temperature.

Anelastic measurements on *hcp* iron under inner-core conditions are not currently possible. Low pressure analogues are commonly used when the deep Earth conditions are too extreme to be accessible experimentally. In doing so, some consideration must be taken for the differences in conditions and chemical behaviour between the analogue and Earth forming phase. No compilations of attenuation mechanisms exist for *hcp*-metals but deformation mechanisms are consistent between *hcp* metals after scaling for the homologous temperature (T/T_M, where T is the temperature and T_M is the melting temperature) and elastic shear modulus [e.g. *Frost and Ashby*, 1982]. Both zinc and *hcp* iron undergo dynamic recrystallisation significantly below their melting temperatures [*Frost and Ashby*, 1982; *Anzellini et al.*, 2013] and deform by both basal and prismatic slip on equivalent slip systems [*Miyagi et al.*, 2008; *Merkel et al.*, 2004; *Yoo and Wei*, 1967; *Yoo et al.*, 2001]. The similarity of deformation mechanism between these and other *hcp* metals [*Yoo and Wei*, 1967] indicates that the crystal structure plays a fundamental role in deformation mechanisms. Anelastic dissipation occurs via processes controlled the by the crystallography (e.g. dislocations, diffusion) and so therefore it is reasonable to assume a first-order similarity is likely to exist between anelastic deformation mechanisms as well.

To address the lack of of anelasticity at seismic frequencies in *hcp*-metals we measured the anelastic response of zinc, at high pressure and up to a homologous temperature of 0.8. The remaining sections of this paper describe the experimental method, an improved approach to data processing needed to extract the anelastic response, the derivation of a model of anelasticity that fits our results, and a discussion of the significant softening observed in the measurements and the implications thereof.

2 Experimental Method

This study utilises the experimental method of *Li and Weidner* [2007] to measure the anelastic response of zinc relative to an elastic reference. Small amplitude sinusoidal strains were applied to an experimental column consisting of a zinc sample and corundum elastic standard, whilst simultaneously acquiring X-radiographic images. Pure-shear strains in the sample and standard were determined by tracking displacement of marker foils in the X-radiographs with an improved image processing algorithm. Strain in the elastic standard is used as a proxy for stress, which combined with the sample strain and the phase lag of the sample relative to that of the elastic standard is sufficient to determine the anelastic response of the sample.

2.1 Samples

Zinc was used as a low-pressure analogue for the *hcp*-iron because of its low melting temperature. Although its ratio of the a to c axis lengths is non-ideal (at 1.87), and very different from that of *hcp*-iron [1.50-1.62, *Fischer and Campbell*, 2015], unlike other ambient pressure *hcp* metals, it is not inflammable (e.g. magnesium) or toxic (e.g. cadmium).

Two different samples were used in this study. A sample of 1 mm diameter high purity zinc wire (99.9985 % metal basis, Puratronic from Alfa Aesar) and a sample of fine grained zinc powder (99% metal basis, particle size: −200 mesh (75 µm) that had not been stored in an inert atmosphere) from Sigma Aldrich; hereafter referred to as 'wire' and 'powder' samples respectively. The wire samples were prepared by polishing pieces of wire to ~1 – 1.3 mm lengths and the powder samples were pressed into similarly long, 1 mm diameter pellets in a steel die with flat ended pins. High-resolution X-ray diffraction of the zinc powder shows it to contain trace amounts of two forms of ZnO (cubic and hexagonal) and at least one form of $Zn(OH)_2$.

The elastic standards were 1 mm diameter solid rods of Alsint-23 corundum, from Alfa Aesar. Each piece was polished to <0.9 mm long with flat parallel ends. Two pieces were used on either end of the zinc samples in the experiments to keep the cell symmetrical and to guarantee that at least one standard could be observed in the X-radiographs. Disks of 25 µm thick platinum foil were used as markers between the samples and corundum standards as well as at the outer ends of the corundum standards.

2.2 Experimental procedure

The sample and standard were enclosed in a cubic assembly and loaded into the the D-DIA [*Durham et al.*, 2002; *Wang et al.*, 2003] on beam-line X17B2 at the NSLS, Brookhaven National Laboratory, New York. The sample assembly for the experiments consisted of a 6.1 mm cube of pyrophyllite baked to 1000°C with a 3 mm diameter hole drilled through it. This hole contained a crushable alumina sleeve, 2.36 mm outer, 2.10 mm inner diameter graphite furnace and a 1.8 mm outer diameter, 1.0 mm inner diameter, 3 mm long boron nitride sleeve. The sample stack was inserted into this boron nitride sleeve and capped at the ends by crushable alumina. A C-type thermocouple inside a 0.8 mm diameter 4-bore alumina rod was inserted radially with its hot junction just inside the furnace and did not touch the sample. A cross-section of the same cell assembly used here is included in *Dobson et al.* [2012].

Before each experiment was compressed, the 10-element energy dispersive X-ray diffraction detector [*Weidner et al.*, 2010] was calibrated using a corundum standard, with 10 minute exposure, and open press measurements were taken from both the zinc and corundum samples, with 5 minute exposures. Each experiment was compressed to 240 kN (27 short-tons force) over ~2 hours. After heating to the desired temperature, further diffraction patterns were acquired from both sample and standard. The zinc diffraction volume was in the centre of the sample and that of the corundum in the part closest to the zinc. The samples were then strained sinusoidally at periods of 10, 30, 100 and 300 s by driving the D-DIA's deformation pumps. We were not able to acquire shorter period data due to the mechanical limits of the D-DIA system and time constraints prevented the acquisition of data with longer periods. The amplitude of the deformation was the minimum needed to robustly observe sinusoidal strains in both the sample and elastic standard. During each deformation experiment, X-radiographs were acquired using a YAG scintillator and a visible light camera, for a minimum of 10 nominal periods. Between 20 and 40 X-radiographs were collected per driving period, with an exposure time of 0.3 s. A typical radiograph is shown in Figure 1. After all data had been acquired at each temperature, the temperature was changed and the cycle repeated. Data was acquired during both increasing and decreasing temperature steps, to confirm that the results are not affected by the thermal history of the sample. The maximum temperature at which the data reported here was collected was 400 °C (a homologous temperature of ~0.8).

A further experiment was performed to confirm there are no significant temperature differences between the thermocouple, sample and corundum standard. This experiment used the melting curve of zinc as an indenpendent constraint and the measured pressure and temperature were within error of the melting curve when the zinc sample melted. Full details of the experiment are included in Appendix A.

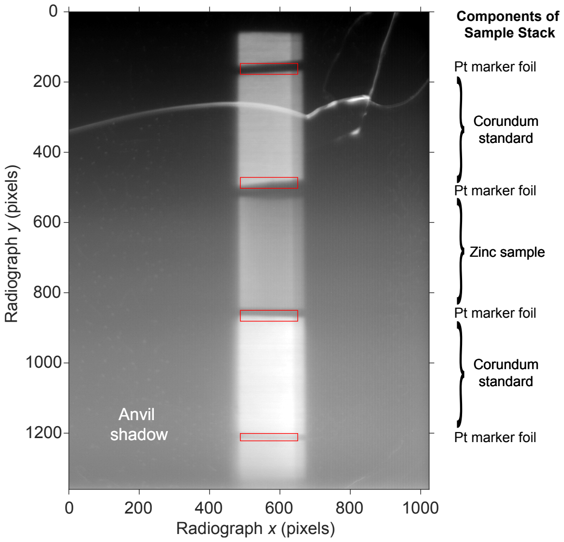

Figure 1. Annotated example X-radiograph from Zinc powder experiment (Zn_08), at 240 kN, 117 °C and 100 s period. The bright stripe in the center of the image contains the sample and corundum standards, as annotated on the right hand side. The red boxes are the positions of the regions of interest tracked between images. The dark areas at either side of the image are the shadows of the Tungsten Carbide anvils and the bright curved cross-cutting feature in the top third of the image is a crack in the YAG scintillator. The scale of the image is 2 µm/pixel.

After each sinusoidal deformation experiment the samples were recovered, mounted in epoxy resin and polished for analysis in the FEI Quanta 650 field emission gun (FEG) scanning electron microscope at the University of Leeds. A sample of the untempered zinc wire was also prepared for analysis. The final finish was a 0.03 µm colloidal silica chemo-mechanical polish in an alkaline solution [*Lloyd*, 1987]. Electron Back-Scatter Diffraction (EBSD) measurements were obtained using a 20 kV accelerating voltage, a spot size of 65 and with a 27 mm working distance. The step size was 3.5 µm for the as-drawn wire and 1 µm for the experimental samples. The Kikuchi patterns were automatically indexed using Oxford Instrument's AZtec software package. Only zinc metal was listed as a possible phase during indexing.

Analysis of the EBSD data was performed using MTEX [*Bachmann et al.*, 2010, 2011]. Grain reconstruction was performed with the threshold misorientation-angle, that indicates a grain boundary, set at 5° and a minimum grain-size of 10 pixels. Orientation Distribution Functions (ODFs), used to plot pole figures, were calculated with a kernel half width of 4°. These values give reasonably robust grain-segmentation and changing the threshold to 10° does not significantly change the grain-size or grain-grain misorientation distributions but it does result in an increase the maximum misorientation within a single grain.

2.3 Diffraction pattern analysis

The pressure in the experiments was determined from the corundum diffraction patterns because above ~200°C the zinc recrystallised rapidly and its diffraction patterns ceased to reliably contain multiple zinc diffraction peaks and individual peaks would rapidly increase and decrease in intensity. The combination of rapid recrystallisation and energy dispersive X-ray diffraction resulted in most zinc diffraction patterns containing too few peaks to adequately constrain differential pressure or differential stress.

At each pressure–temperature condition there are 10 diffraction patterns, corresponding to each element of the detector. The first 9 corundum diffraction peaks were fitted in each pattern using Plot85 and fit to determine the unit cell volume. Volume strains were calculated independently for each of the detector elements using the corresponding open-press unit cell volume, the corundum thermal expansion coefficients of *Fei* [1995] and the temperature reported by the thermocouple. There was no significant temperature offset between the corundum and thermocouple as confirmed using the melting curve as an independent constraint (see Appendix A).

Pressure was calculated from the volume strains, assuming a bulk modulus of $K_0 = 254.28\,\mathrm{GPa}$ with pressure and temperature derivatives of $K' = 4.27$ and $\mathrm{d}K/\mathrm{d}T = -0.0173\,\mathrm{GPa\,K^{-1}}$ respectively. The bulk modulus and the temperature derivative are a linear fit to the Voigt-Reuss-Hill average bulk modulus of *Goto et al.* [1989]'s elastic stiffnesses (c_{ij}s). The pressure derivative was calculated from the pressure dependencies of the elastic stiffnesses of *Gieske and Barsch* [1968], assuming the derivatives are linear at pressures greater than 1 GPa. The elastic stiffnesses were used to derive the equation of state values from in order to be consistent with the Young's moduli calculated subsequently. The pressures reported in Table 2 are the weighted mean and standard deviation of the values calculated from all the detector elements.

3 X-Radiograph Analysis

In order to determine the anelasticity of zinc we need to track the amplitude and phase of strain in the zinc and corundum (used as a proxy for stress) during the experiment. To do so with sufficient precision we had to develop an improved analysis method for processing the sequences of X-radiographs collected during sinusoidal deformation.

3.1 Prior work

The algorithm used here, for sub-pixel tracking of marker foil displacements in X-radiographs, was initially implemented by *Li et al.* [2003] and is based on the image processing algorithms of *Pratt* [1991] and *Trucco and Verri* [1998]. The basis of the algorithm is calculating the Sum Squared Differences (SSD) of the pixel intensity values between a region of interest in a reference image ($R_r[i, j]$) and a search region in the subsequent image ($R_s[i, j]$):

$$D_o = \sum_i \sum_j (R_r[i, j] - R_s[i, j + o])^2 \tag{1}$$

where D_o is the intensity SSD between the two images, at an offset of o pixels. The displacement of the region of interest, and hence the marker foil, was found with subpixel resolution by finding the minimum of a cubic spline interpolated between the values of D_o. The offset range used to determine the displacement is generally ±5 pixels (10 µm) vertically in the image (y-direction in Figure 1). *Li et al.* [2003] were primarily interested in tracking comparatively large total displacements (0-10 pixels) during deformation experiments and tracked the displacement between consecutive pairs of images ($[R_1, R_2]$, $[R_2, R_3]$, $[R_3, R_4]$...). They calculated the length change and strain in their samples by combining the displacements of two regions of interest above and below the sample.

Dobson et al. [2008, 2010] used the same approach to measure small sinusoidally varying displacements during thermal conductivity experiments. *Hunt et al.* [2011, 2012] improved the precision in similar experiments by using the central radiograph in 100–1000 image long time series as a single reference ($[R_r, R_1]$, $[R_r, R_2]$, $[R_r, R_3]$, $[R_r, R_4]$...) and utilising a degree 6 polynomial rather than a spline to find the minimum of the SSD. These studies were primarily interested in the phase differences and not specifically concerned with the amplitude of the sinusoidal displacements. In this study, good constraints on both the amplitude and phase of the strain are critical. Both the original and improved algorithms returned signals that were too variable for the reliable extraction of anelastic properties. We have therefore further refined the algorithm to return more consistent and precise displacements of the marker foils.

3.2 Refined algorithm

To gain precision in the image processing, rather than treating each pair of images in isolation and then interrogating the displacements, we describe all the SSD ($D_{o,t}$, Equation 1) for a sequence of images (Figure 2a), as a single polynomial surface, $S_{o,t}$. The surface has degree m in offset (o), n in time (t) and the degree of the polynomial surface is the greater of m and n [*Gallier*, 2000]. For $m > n$, the surface is:

$$S_{o,t} = \sum_{g=0}^{m} \sum_{h=0}^{\min(n,m-g)} p_{gh}\, o'^{g}\, t^{h}, \tag{2a}$$

where p_{gh} is a polynomial coefficient,

$$o' = o_t + a \sin(ft + \phi), \tag{2b}$$

and a is the amplitude, ϕ is the phase and f is the frequency of the displacement.

The surface, $S_{o,t}$, is fit to $D_{o,t}$ by ordinary least squares minimisation. The fit is performed simultaneously for all the regions of interest with independent surface coefficients for each region of interest and the period of the driving force as the only common parameter. For the temperature step experiments, with sequences longer than 200 images, $m = 6$ and $n = 3$ were found to be sufficient to reproduce the shape of the SSD surface and capture the displacement's phase and amplitude. It was found that smaller degree surfaces do not fully capture the shape of the $D_{o,t}$ surface while higher degree surfaces have artefacts in the fit. Figure 2a plots the $D_{o,t}$ values from one region of interest in a data set of 400 radiographs. This clearly shows the significant increase in SSD with offset and the sinusoidal displacements of the marker foil with time. Figure 2b is the fitted surface, $S_{o,t}$, and Figure 2c shows the residuals between $D_{o,t}$ and $S_{o,t}$ (Equation 2). The formal errors in the period, phase and amplitude in the surface fit are typically 0.002 s, 0.01 radians and 0.001 pixels respectively and, for the 300 s data, up to 3 orders of magnitude smaller than those for the previous fitting method (Section 3.1).

The least squares residuals form a bow-tie shape in offset (Figure 2c). This is because at small offsets the intensity differences are small and the addition of noise to small differences squared has less effect than at large offsets where the intensity differences are larger. For example, the addition of 1 arbitrary unit of noise to an intensity difference of 3

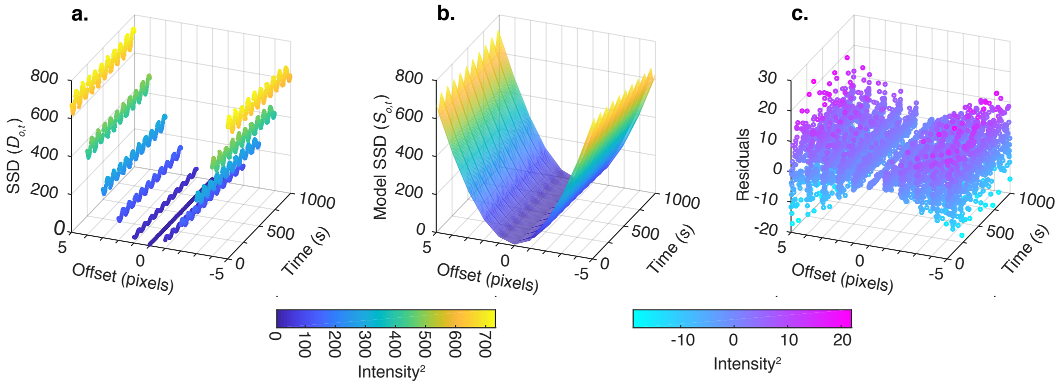

Figure 2. Example fit of SSD data with the improved algorithm. (a) Sum differences squared data ($D_{o,t}$) for the first (top) region of interest plotted against time from Zinc powder experiment (Zn_08), at 27 short-tons force and ~100°C with 100 s period. (b) the best fit surface ($S_{o,t}$) to the data and (c) the residuals.

increases the difference squared from 9 to 16 (difference of 7) whereas 1 arbitrary unit to an intensity difference of 10 increases the difference squared from 100 to 132 (difference of 32).

The absolute position of each region of interest (P_t) is the minimum of the surface with respect to time:

$$P_t = (\partial S_{o,t} / \partial o = 0),$$

which was found by differentiation of the surface polynomial. The length of the samples is the difference in position of P_t for the region of interest above and below the sample, accounting for the phase angle of the driving wave at the time of the reference radiograph.

The largest source of error is the absolute length of the sample, which *Li et al.* [2003] argued to be ±5 pixels. To minimise both the absolute and relative length error between data acquisitions, the regions of interest were automatically selected. Horizontally the regions of interest were centred in the bright part of the image and ended close to but not overlapping with the anvil shadows. The regions of interest not adjacent to the zinc sample (Figure 1, top and bottom red boxes) were centred over the minimum in a spline interpolation of the intensity profile; the width and depth of which remained very similar throughout the experiment. The regions of interest adjacent to the zinc sample became broader throughout the experiment as the platinum marker foil diffused into the zinc. To account for this the regions of interest were centred over the maximum gradient (as interpolated by a spline) on the side of the foil away from the sample. The sample lengths were subsequently adjusted to account for the thickness of the platinum foil; half a foil thickness, 12.5 µm or 7 pixels, was subtracted from the lengths of the corundum standards and 25 µm (14 pixels) from the zinc sample length.

Figure 3 shows the length change and our fits for the corundum standard and zinc sample as a function of time, for the same data set used in Figures 1 and 2. The large blue circles highlight the sample length in the reference radiograph; if the reference coincided with either extrema of the sinusoidal wave a small error would be added to the length of the samples and propagated into the subsequent calculations. For the zinc sample, which had a relatively large deformation amplitude, both the method used previously by *Hunt et al.* [2011, 2012] (red lines) and the new method (black lines) are good fits to the length change data and give virtually the same values for a, f and ϕ (Equation 2b). The biggest differences between the data and the fits is at the beginning and end of the time series and arises from how the secular length change is dealt with by the previous methods' fit [see *Hunt et al.*, 2011, 2012, for details]. For the smaller amplitude corundum data the improvements in the fit are more significant. In small amplitude data ((Figure 3a), the new algorithm overcomes the systematic underestimation of amplitude present in the previous algorithm. The new algorithm also returns useable phases and amplitudes from data which was previously too noisy or with too small an amplitude to fit. With the new image analysis method the fitted length change of the bottom elastic standard has an amplitude and phase similar to that of the top elastic standard.

4 Anelastic model

Assuming that the corundum standard is elastic the frequency dependent Young's modulus of the zinc sample is:

$$E = \frac{\varepsilon_{\mathrm{Al_2O_3}}}{\varepsilon_{\mathrm{Zn}}} E_{\mathrm{Al_2O_3}} \tag{3}$$

where ε is the amplitude of the sinusoidal deformation divided by the mean length and $E_{\mathrm{Al_2O_3}}$ is the elastic Young's Modulus of corundum. The strain energy dissipation is:

$$Q^{-1} = 1/\tan^{-1}(\phi_{\mathrm{Al_2O_3}} - \phi_{\mathrm{Zn}}) \tag{4}$$

where the values $\phi_{\mathrm{Al_2O_3}}$ and ϕ_{Zn} are the phase of the length changes in the corundum standard and zinc sample respectively.

We assume that the corundum standard is isotropic and utilised MSAT [*Walker and Wookey*, 2012] to calculate $E_{Al_2O_3}$ as the Voigt-Reuss-Hill average of corundum's elastic stiffnesses at the pressure and temperature conditions reported by the thermocouple and

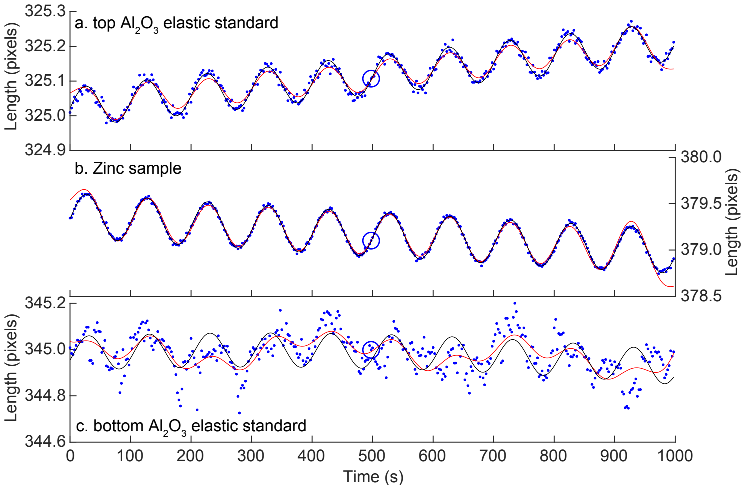

Figure 3. Elastic standard (a, c) and zinc sample lengths (b) calculated by the SSD image analysis for the same data shown in Figures 1 and 2. Blue dots are minima of the SSD polynomial for independent calculations of the displacement between each radiograph and the standard and the red lines are the fit to the minima calculated using the method of *Hunt et al.* [2011, 2012]. The black lines are the length changes calculated from the surface fits to all the SSD data (Figure 2) and thus not not fits to the points, but ideally they should reproduce them. The large blue circles highlight the length in the reference image. The anelastic dissipation was calculated using only the strains from the 'top' corundum standard.

calculated from the diffraction. The elastic stiffnesses were calculated using the ambient condition value and temperature derivatives of *Goto et al.* [1989] and the pressure derivatives of *Gieske and Barsch* [1968], assuming the derivatives are linear at pressures greater than 1 GPa.

The temperature and oscillation period variation in Young's modulus and attenuation can be fit with various models of linear viscoelasticity [Figure 4, e.g. *Sundberg and Cooper*, 2010; *Nowick and Berry*, 1972; *Jackson et al.*, 2000; *Faul and Jackson*, 2015; *Jackson*, 2015]. Each model has different characteristic frequency dependent behaviour that relates the stress, $\sigma(t) = \sigma_0 \exp(i\omega t)$ where $\omega = 2\pi f$, to the strain response, $\varepsilon(t) = \varepsilon_0 \exp(i\omega t - \delta)$, by a loss angle, δ. For each model, the strain response can be obtained by integrating its behaviour over the stress history to compute the dynamic compliance, $J^*(\omega)$ [*Nowick and Berry*, 1972; *Jackson*, 2015]:

$$J^*(\omega) = \frac{\varepsilon(t)}{\sigma(t)} = \mathrm{i}\omega \int_0^\infty J(t) \exp(-\mathrm{i}\omega t)\mathrm{d}t \tag{5}$$

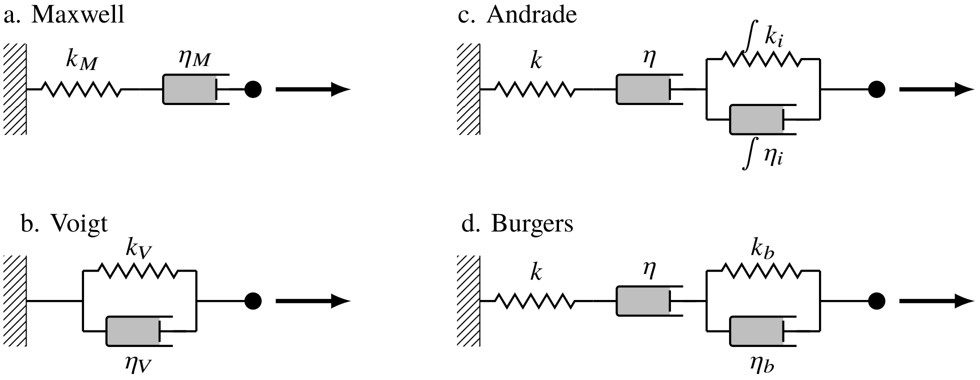

Figure 4. Schematic representations of a. Maxwell, b. Voigt, c. Andrade and d. Burgers models. Springs (labelled k) represent the elastic components of the model and dashpots (labelled η) the viscous component.

Separating the instantaneous (elastic, real) and retarded (viscous or anelastic, imaginary) parts gives:

$$J^*(\omega) = J_1(\omega) - \mathrm{i}J_2(\omega) = J_U + \mathrm{i}\omega \int_0^\infty [J(t) - J_U] \exp(-\mathrm{i}\omega t)\mathrm{d}t \tag{6}$$

where J_U is the unrelaxed compliance and the inverse of the elastic modulus ($J_U = 1/M$). For simple shear torsion experiments, the relevant elastic modulus is the shear modulus (μ) and for the pure shear experiments performed here, M is the Young's modulus (E).

The frequency dependent elastic modulus ($M = E$ or μ) can be determined from the expressions for J_1 and J_2:

$$M(\omega) = [{J_1}^2(\omega) + {J_2}^2(\omega)]^{-1/2} \tag{7}$$

and the associated strain energy dissipation is:

$$Q^{-1}(\omega) = \frac{J_2(\omega)}{J_1(\omega)}. \tag{8}$$

Each viscoelastic dissipation model has different characteristic behaviour and equations. For the Burgers model (Figure 4d) these equations are usually expressed in terms of $J_M(= 1/k_M)$, $J_V(= 1/k_V)$, τ_M and τ_V, where τ is the relaxation time:

$$\tau = k/\eta \tag{9}$$

Separating the independent components simplifies the fitting of models to data. The complex compliance, written in terms of the four independent model components, is [after *Faul and Jackson*, 2015]:

$$J^*(\omega) = \frac{1}{k_M} + \frac{1}{k_V(1 + \mathrm{i}\omega\eta_V/k_V)} - \frac{\mathrm{i}k_V}{\omega\eta_V}$$

which rearranges to:

$$J_1(\omega) = \frac{1}{k_M} + \frac{1}{k_V(1 + \omega^2\eta_V^2/k_V^2)} \tag{10a}$$

$$J_2(\omega) = \frac{\omega\eta_V}{k_V^2(1 + \omega^2\eta_V^2/k_V^2)} - \frac{k_V}{\omega\eta_V} \tag{10b}$$

where k_M and k_V are the respective spring constants of the Maxwell and Voigt components of the Burgers model and η_M and η_V are the corresponding dashpot viscosities. The equivalent complex compliance expressions for the Maxwell and Andrade models are in Appendices B and C respectively.

The experimental Young's moduli and Q^{-1} data (Equations 3 and 4) were fit with a two component Maxwell and four component Andrade and Burgers models of anelasticity. There is not sufficient density or range of frequencies in this study's data to fit more complex viscoelastic models, e.g. a generalised Burgers model with its normalised distribution of anelastic relaxation times [e.g. *Anderson and Minster*, 1979]. The data at each temperature was fit independently by simultaneously minimising the unweighted normalised residuals for both $E(\omega)$ and $Q^{-1}(\omega)$ (Equations 7 and 8). The parameters solved for in the fitting were the elastic (k) and viscous (η) components of the anelastic models (Equation 10). This ensures, as far as possible, that the model parameters are independent of each other, which is not the case when the relaxation time, τ (Equation 9), is one of the fitted parameters.

By assuming negligible pressure derivatives and a functional form for the temperature dependency of each model parameter, it was possible to simultaneously fit all the data for each experiment with a Burgers model of anelasticity. A linear temperature dependency was assumed for E_M. The viscosities (η_M and η_V) were assumed to have Arrhenius temperature dependencies ($\ln \eta(T) = a + b/RT$). The temperature dependency of E_V was less clear because with a linear temperature dependency, which is reasonable for an elastic process, the values of E_V become negative at high temperatures. A number of alternative functions were tested but an Arrhenius temperature dependency was used because it both approximated the data and remained physically reasonable.

5 Results

A number of sinusoidal deformation experiments were performed for this study, the results from which were consistent but in some cases subject to significant scatter, especially in the phase lag ($\phi_{\mathrm{Al_2O_3}} - \phi_{\mathrm{Zn}}$, Equation 4). We suspect this scatter is due at least in part to geometrical imperfection in some of the sample assemblies and we have excluded the most significantly effected experiments from our analysis. We thus focus on the results from the two experiments with the least scatter, one of which had a sample of zinc wire and the other zinc powder. It is not possible to determine how imperfect the experimental geometry is from the radiographs because most of the assembly is obscured by the anvils (Figure 1) but the geometry of the powder experiment is more ideal than that of the wire experiment because in the latter the thermocouple tip can just be seen protruding into the anvil gap.

The frequency dependent Young's modulus ($E(\omega)$, Figure 5) and dissipation ($Q^{-1}(\omega)$, Figure 6) of the two samples were calculated from the experimental observations listed in Table 1. The typical strains in both the sample ($\sim 5 \times 10^{-4}$) and the standard ($\sim 1 \times 10^{-4}$) are smaller than the typical strains measured by *Li and Weidner* [2007] but large compared to the strains used in previous low-pressure anelastic measurements [$2 \times 10^{-6} - 2 \times 10^{-5}$, e.g. *Jackson et al.*, 2000]. The corundum strain implies stress amplitudes ranging from 110 to 374 MPa, with a mean of 240 MPa.

The data shows a decrease in Young's modulus and increase in dissipation with oscillation period, as expected for a sample with viscoelastic behaviour (Figures 5a,b). The change in E and Q^{-1} with temperature and oscillation period is greater in the wire (Figures 5a and 6a) than the powder (Figures 5b and 6b). The $E(\omega)$ data are predominantly smaller than the isotropic average elastic Young's moduli, here defined as the average of a uniform random distribution of zinc crystal orientations (solid black lines in Figure 5). All the data fall between the maximum and minimum possible Young's moduli, which are defined here as the maximum and minimum possible moduli for variation in the straining direction of a zinc single crystal (dashed black lines in Figure 5). The Young's moduli were calculated in MSAT [*Walker and Wookey*, 2012] using the ambient condition and temperature dependencies of the elastic stiffnesses (c_{ij}s) of *Alers and Neighbours* [1958] and the pressure derivatives of *Srinivasan and Rao* [1971] as compiled by *Ledbetter* [1977].

There is no significant offset between the data collected before and after the maximum temperature in each experiment (open vs. filled symbols in Figures 5 and 6; Table 1 lists the data in order of collection). The relatively large change in pressure between the

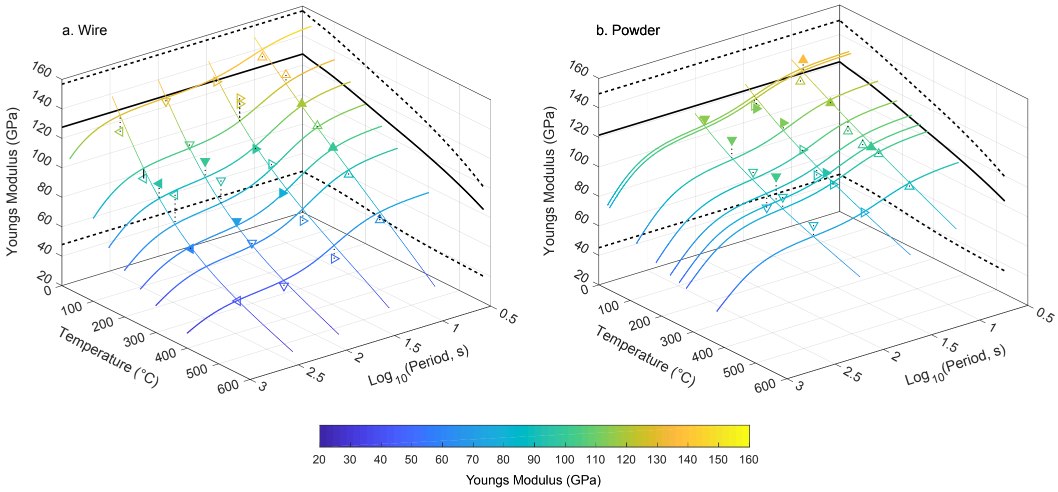

Figure 5. Young's modulus of the Zinc (a) wire and (b) powder samples plotted against temperature and period. The open symbols are the data collected before the maximum temperature of the experiment and the filled symbols after; for the order of the data collection see Table 1. Error bars have been excluded for clarity; the median error in the Young's modulus for both data sets is 10.1 GPa. Dotted lines connect the data to the corresponding point in the fitted plane. The solid lines are the global Burgers model fit to the data and plotted at the nominal periods and temperatures of the measurements. Solid black line in the back planes is the Young's modulus calculated from a Voigt-Reuss-Hill average of the zinc c_{ij}s and the dashed lines are the maximum and minimum possible Youngs modulae from the c_{ij}s. All lines terminate at the melting temperature.

first and last data sets (Table 1) has no discernible effect on the data implying pressure derivatives close to zero.

Fitting the data with a Maxwell (Equation B.2) or Andrade (Equation C.2) model did not produce reasonable fits to the data. Neither models can reproduce the inflection in the dissipation data with frequency (Figure 6a) and the best fitting Maxwell model requires a frequency dependent viscosity. The Andrade model fit prefers the micro-creep coefficient (n, Equation C.2) to be > 200. This is much greater than the generally accepted value of $n \sim 1/3$ garnered from mirco-creep data [e.g. *Sundberg and Cooper*, 2010] and which has also been observed in creep of zinc [*Cottrell and Aytekin*, 1947]. The Burgers model (Equation 10), on the other hand, produces a reasonable fit to the data and captures its major features, specifically the decrease in $E(\omega)$ with temperature and period as well as the shape of the dissipation data. The Burgers model parameters calculated independently at each temperature are plotted in Figure 7 and listed in Table 2.

Group	Temperature	Pressure	Period	Strain Amplitude		Phase Lag	$E_{Al_2O_3}$
				Zinc	Al_2O_3	$\phi_{Al_2O_3} - \phi_{Zn}$	
	(°C)	(GPa)	(s)	($\varepsilon \times 10^6$)	($\varepsilon \times 10^6$)	(degrees)	(GPa)
Zn_02, Wire Sample							
1	25	4.8±0.8	299.9 ± 1E-08	687 ± 3E-03	188 ± 4E-03	12.4 ± 2E-04	425.4
			100.4 ± 0.001	658 ± 4	198 ± 5	4.3 ± 0.5	
			30.0 ± 0.003	545 ± 2	168 ± 2	4.8 ± 1.2	
			10.0 ± 0.002	261 ± 1	84 ± 2	5.5 ± 1.8	
2	100	4.8±0.8	299.4 ± 9E-09	784 ± 2E-03	172 ± 3E-03	20.5 ± 3E-04	422.5
			100.0 ± 0.001	693 ± 6	175 ± 7	9.6 ± 0.8	
			30.2 ± 0.005	554 ± 3	167 ± 3	6.5 ± 1.3	
			30.1 ± 0.003	558 ± 2	164 ± 2	7.0 ± 0.9	
			10.0 ± 0.002	264 ± 2	84 ± 2	4.4 ± 1.7	
3	200	4.2±0.4	299.8 ± 7E-09	872 ± 2E-03	194 ± 2E-03	17.4 ± 2E-04	414.7
			100.1 ± 0.001	820 ± 3	183 ± 3	11.0 ± 0.3	
			29.9 ± 0.004	645 ± 3	145 ± 3	9.6 ± 1.6	
			10.0 ± 0.002	300 ± 2	79 ± 2	7.2 ± 2.0	
4	300	4.2±0.4	300.0 ± 2E-08	882 ± 2E-03	164 ± 3E-03	19.7 ± 2E-04	409.4
			100.9 ± 0.002	840 ± 4	125 ± 9	21.5 ± 1.7	
			29.9 ± 0.003	675 ± 2	108 ± 3	13.1 ± 2.1	
			10.0 ± 0.002	308 ± 1	66 ± 3	6.9 ± 2.8	
5	400	4.1±0.6	299.8 ± 4E-08	928 ± 8E-03	96 ± 1E-02	23.2 ± 2E-03	403.5
			99.4 ± 0.001	875 ± 5	92 ± 8	17.9 ± 1.8	
			30.0 ± 0.003	712 ± 2	89 ± 4	18.7 ± 2.5	
			10.0 ± 0.002	331 ± 2	55 ± 3	11.6 ± 3.2	
6	250	3.4±0.6	300.8 ± 2E-08	850 ± 7E-03	127 ± 9E-03	17.3 ± 1E-03	408.2
			99.9 ± 0.001	823 ± 4	142 ± 5	18.6 ± 0.7	
			33.5 ± 0.063	580 ± 11	114 ± 14	9.9 ± 8.5	
			10.0 ± 0.002	307 ± 2	75 ± 3	11.9 ± 2.3	
7	150	3.3±0.9	301.4 ± 1E-08	800 ± 1E-02	184 ± 2E-02	14.0 ± 1E-03	412.8
			100.3 ± 0.001	764 ± 10	186 ± 10	10.0 ± 0.9	
			30.0 ± 0.004	638 ± 4	152 ± 4	8.6 ± 1.7	
			10.0 ± 0.002	308 ± 3	89 ± 3	6.4 ± 2.1	
Zn_08, Powder Sample							
1	28	2.6±0.6	10.0 ± 0.001	272 ± 3	79 ± 3	2.9 ± 2.2	415.3
			30.0 ± 0.002	575 ± 3	158 ± 3	5.3 ± 1.2	
			99.9 ± 0.012	692 ± 4	191 ± 3	5.6 ± 1.3	
2	182	3.7±0.7	10.0 ± 0.001	319 ± 3	80 ± 3	8.7 ± 2.3	413.2
			30.0 ± 0.002	628 ± 3	153 ± 2	10.8 ± 1.2	
			99.5 ± 4E-05	747 ± 55	174 ± 43	10.6 ± 2.8	
3	227	3.6±1.5	10.0 ± 0.001	312 ± 3	75 ± 3	3.2 ± 2.4	410.4
			30.0 ± 0.002	623 ± 4	134 ± 3	7.7 ± 1.6	
			99.9 ± 0.012	747 ± 4	139 ± 3	13.7 ± 1.7	
4	279	3.7±0.5	10.0 ± 0.001	305 ± 3	74 ± 3	6.1 ± 2.4	408.0
			30.0 ± 0.002	611 ± 3	131 ± 3	9.6 ± 1.4	
			99.9 ± 0.012	729 ± 4	160 ± 3	9.4 ± 1.6	
5	377	3.4±0.4	10.0 ± 0.001	306 ± 3	66 ± 3	4.3 ± 3.1	401.8
			30.0 ± 0.002	610 ± 3	120 ± 2	10.8 ± 1.6	
			100.0 ± 0.012	713 ± 4	143 ± 3	12.4 ± 1.6	
6	34	2.5±0.6	10.0 ± 0.001	270 ± 3	89 ± 3	3.7 ± 2.1	414.6
			30.0 ± 0.003	554 ± 3	151 ± 3	8.8 ± 1.4	
			100.0 ± 0.003	664 ± 4	186 ± 3	11.4 ± 0.9	
7	256	2.7±3.6	10.0 ± 0.001	285 ± 2	71 ± 2	6.0 ± 2.4	404.8
			30.0 ± 0.002	562 ± 3	129 ± 2	8.7 ± 1.4	
			100.0 ± 0.007	667 ± 8	166 ± 7	19.0 ± 2.3	
8	120	2.9±0.8	10.0 ± 0.001	276 ± 3	78 ± 3	3.2 ± 2.5	412.7
			30.0 ± 0.002	545 ± 3	148 ± 2	4.4 ± 1.2	
			100.1 ± 0.003	658 ± 3	177 ± 3	6.3 ± 0.9	

Table 1. Experimental conditions and strain data from the two experiments in this study. The data for each experiment are presented in the order in which they were collected. The data in Figures 5 and 6 are calculated from this data using Equations 3 and 4. The values of $E_{Al_2O_3}$ are those used in the calculations and were calculated as described in the text. For Zn_08 the Al_2O_3 strains are those of the 'top' elastic reference (Figure 3) whilst in Zn_02 only one corundum standard was imaged.

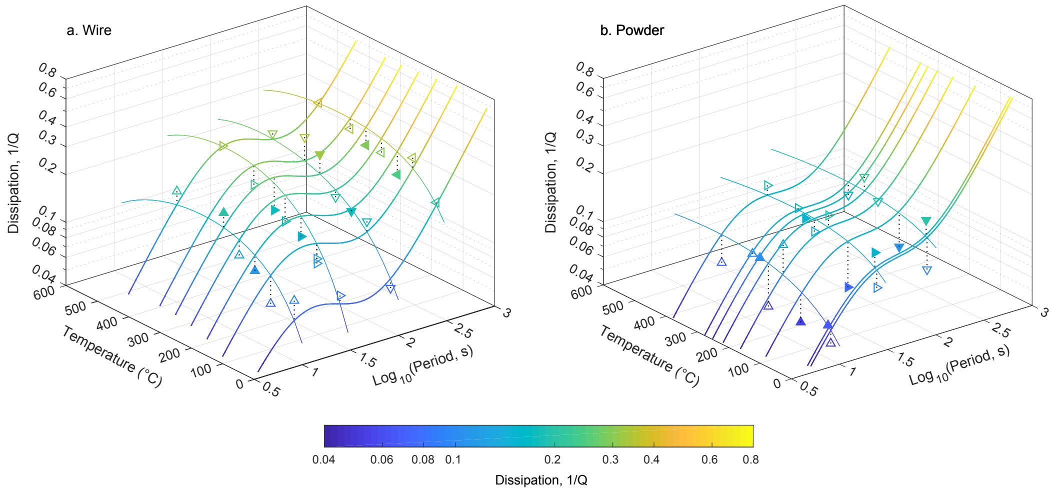

Figure 6. Dissipation in the Zinc (a) wire and (b) power samples plotted on a log scale against temperature and period. The open symbols are the data collected before the maximum temperature of the experiment and the filled symbols after; for the order of the data collection see Table 1. Error bars have been excluded for clarity. Dotted lines connect the data to the corresponding point in the fitted plane. The solid lines are the global Burgers model fit to the data and plotted at the nominal period and temperatures of the measurements. All lines terminate at the melting temperature. Note the directions of the temperature and period axes are reversed relative to Figure 5.

Using the assumed temperature dependencies for each Burgers model parameter a global model was fit to all the data in each experiment. The global models are plotted with the data in Figures 5 and 6. These are a reasonable fit to the data, reproducing its major features. The temperature dependent model parameters are listed in Table 3 along with the functional forms used, and plotted in Figure 7. The global models closely match the parameters calculated independently at each separate temperature.

The temperature dependency of the infinite frequency Young's modulus (E_M) are approximately linear in temperature (Figure 7a). The values are similar between the two samples and there is some overlap of the individual values. The calculated temperature derivatives (Table 3) are different by more than two standard errors of each other and only the powder sample's temperature derivative is within error of that of the elastic values derived from the stiffnesses (dE/dT = $-0.07\,\mathrm{MPa\,K^{-1}}$). The values for E_M are all close to the isotropic elastic Young's modulus and within the maximum and minimum bounds.

There are a number of possible causes for the higher than expected temperature derivative. Anelastic softening and dissipation in the corundum standard would increase

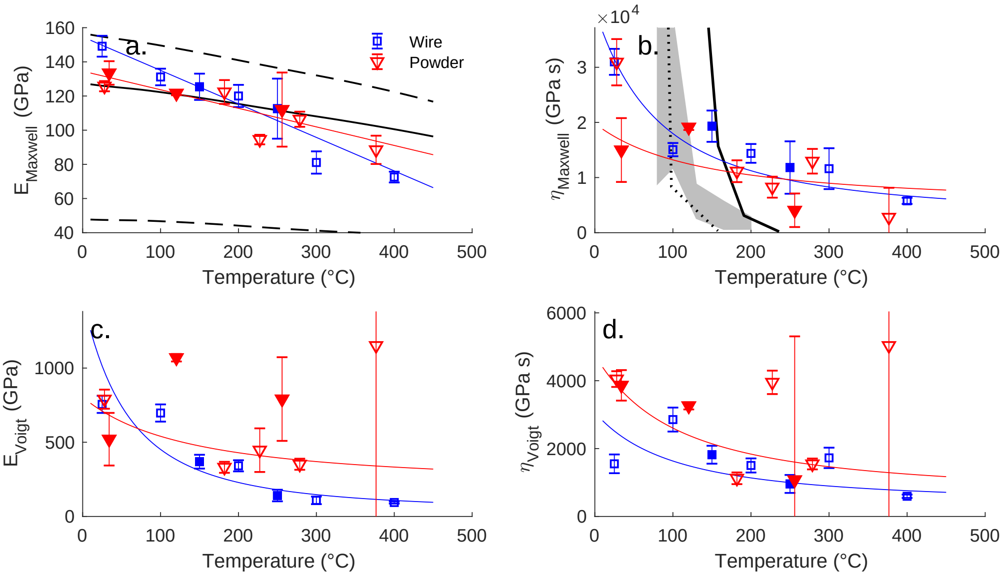

Figure 7. Burgers model parameters plotted against temperature. The symbols are the Burgers fit to the data at each temperature only; the blue squares denote the wire sample and the red triangles are for powder sample. The open symbols are the data collected before the maximum temperature of the experiment and the filled symbols after. Red and blue lines are from the fit to all the data assuming the temperature derivatives listed in Table 3. In a. the solid black line is the isotropic elastic Young's modulus of zinc at the average pressure of the wire experiment (4.1 GPa), the dashed lines are the maximum and minimum possible elastic Young's moduli calculated in MSAT [*Walker and Wookey*, 2012]. In b. the solid black line, dashed black line and grey area are viscosities derived from *Tegart and Sherby* [1958], *Thompson* [1955] and *Murthy and Sastry* [1982] respectively.

Group	Temp	Data used Nominal Period (s)				Pressure	E_M	η_M	E_V	η_M	Maxwell time
	(°C)	10	30	100	300	(GPa)	(GPa)	(10^3 GPa s)	(GPa)	(GPa s)	(s)
Zn_02, Wire Sample											
1	25	y	y	y	y	4.8 (8)	149 (6)	31.0 (24)	755 (58)	1551 (276)	2.1 (4)
2	100	y	y	y	y	4.8 (8)	131 (5)	15.1 (12)	697 (58)	2855 (353)	4.1 (5)
3	200	y	y	y	y	4.2 (4)	120 (6)	14.4 (17)	341 (38)	1503 (208)	4.4 (6)
4	300	E	y	y	Q	4.2 (4)	81 (7)	11.6 (37)	109 (26)	1726 (301)	15.9 (29)
5	400	y	y	y	y	4.1 (6)	73 (3)	5.8 (6)	94 (7)	595 (51)	6.3 (6)
6	250	y	y	y	y	3.4 (6)	113 (18)	11.8 (48)	141 (39)	958 (265)	6.8 (19)
7	150	y	y	y	y	3.3 (9)	125 (8)	19.3 (28)	369 (46)	1819 (264)	4.9 (7)
Zn_08, Powder Sample											
1	28	y	y	y		2.6 (6)	126 (3)	30.9 (42)	790 (64)	4049 (232)	5.1 (3)
2	182	y	y	y		3.7 (7)	122 (7)	11.2 (20)	331 (37)	1125 (172)	3.4 (5)
3	227	y	y	y		3.6 (15)	95 (3)	8.3 (19)	447 (147)	3952 (345)	8.8 (8)
4	279	y	y	y		3.7 (5)	106 (4)	13.0 (22)	352 (37)	1547 (160)	4.4 (5)
5	377	y	y	E		3.4 (4)	88 (8)	2.8 (54)	1151 (8514)	5034 (12939)	4.4 (112)
6	34	y	y	y		2.5 (6)	134 (7)	15.0 (58)	521 (177)	3864 (450)	7.4 (9)
7	256	y	y	E		2.7 (36)	112 (22)	4.1 (30)	791 (282)	1079 (4228)	1.4 (53)
8	120	y	y	y		2.9 (8)	122 (1)	19.1 (5)	1070 (25)	3259 (105)	3.0 (1)

Table 2. Burgers model fits to the data for each temperature conditions. The Data Used columns denote what data was used from each nominal period in calculating Burgers parameters; y – both data used, E - only E, Q - only Q. The Maxwell time (τ) is equal to η_V/E_V (Equation 9).

Constant	Temperature dependency	Intercept (p_0)	Slope (p')
Zn_02, Wire Sample			
E_M	$p_0 + p'.T$	154.6±9.1 GPa	-0.196±0.031 GPa K^{-1}
η_M	$\exp(p_0 + p'/R(T + 273))$	7.6±0.3	6889±1058 J mol^{-1} K^{-1}
E_V	$\exp(p_0 + p'/R(T + 273))$	29.0±2.6	1199±108 K^{-1}
η_V	$\exp(p_0 + p'/R(T + 273))$	5.7±0.4	5331±1385 J mol^{-1} K^{-1}
Zn_08, Powder Sample			
E_M	$p_0 + p'.T$	134.6±10.7GPa	-0.109±0.045 GPa K^{-1}
η_M	$\exp(p_0 + p'/R(T + 273))$	8.4±0.8	3433±2688 J mol^{-1} K^{-1}
E_V	$\exp(p_0 + p'/R(T + 273))$	5.2±0.6	405±259 K^{-1}
η_V	$\exp(p_0 + p'/R(T + 273))$	6.2±0.5	5111±1727 J mol^{-1} K^{-1}

Table 3. Global Burgers model fit to the data listed in Table 2. Temperatures are in celsius.

the apparent temperature derivative but this is deemed unlikely to be significant because other studies do not observe significant anelastic behaviour in corundum [*Li and Weidner*, 2007]. It is more likely that deviations from the ideal experimental geometry have affected the measurements. In the wire experiment, the tip of the thermocouple protrudes further than is ideal into the sample space and this experiment has the temperature derivative of the Young's modulus further from the elastic value. We note here that zinc is very soft and a number of experiments performed during this study failed because the zinc sample extruded from the sample space or deformed significantly during compression. There is also the possibility that anelastic effects not captured by the Burgers model will skew the calculated values but this cannot be tested here.

The creep viscosities (η_M, Figure 7b, Table 3) are within two standard deviations of each other and exhibit an Arrhenius relationship between viscosity and inverse temperature. The viscosities are similar in magnitude to values from creep experiments on high purity zinc by *Murthy and Sastry* [1982] and *Tegart and Sherby* [1958], although they reduce with temperature much more slowly. The activation energies for creep in the wire and powder (6.8(11) and 3.4(27) kJ/mol respectively) are much smaller than the activation energies for creep by dislocation climb or basal slip in zinc [88 and 159 kJ/mol respectivley, *Tegart and Sherby*, 1958] or implied by the creep data of *Murthy and Sastry* [1982]. The values here are also significantly smaller than the activation energy for self diffusion in zinc [96.3 kJ/mol, *Chabildas and Gilder*, 1972] or grain-boundary sliding [*Watanabe et al.*, 1984, 40 – 100 kJ/mol in zinc bicrystals,].

The functional forms of the Voigt elements of the model are less clear and more scattered than those of the Maxwell elements. For both elements an Arrhenius temperature dependency was assumed because other functional forms gave unphysical results or did not describe the data well. The values of the two parameters are similar between the experiments but those from the powder sample tend to be slightly greater than from the wire sample. The value of η_V is an order of magnitude less than that of η_M. Conversely, at all temperatures, the values of anelastic spring component (E_V) are much greater than the pure elastic component (E_M).

Overall the parameters between the two samples are similar enough to imply the same physical process is causing the attenuation in both samples and that the sample histories (i.e. wire vs. compressed powder) do not have a distinguishable effect on the measurements. The small differences between the two sets of parameters are caused by imperfections in the experimental geometries.

5.1 Recovered Microstructures

The inferred sameness of the anelasitic dissipation mechanism in the two experiments is reflected in the similarity of the recovered microstructures (Figures 8 and 9). The two recovered samples have similar grain-sizes (Figures 8d, 8g and 9a) and Lattice Preferred Orientation (LPO, Figures 8f and 8i) even though the wire sample started the experiment with significantly greater grain-size (Figure 8a, 9a) than the -200 mesh (75 µm) particle size powder and presumably a different LPO. The grains in the recovered samples are not equilibrium shapes with some grains having concave boundaries. The samples also contains a small number of quadruple-grain junctions which is consistent with some contribution from grain-boundary sliding.

The LPO of the two recovered samples (Figures 8f and 8i) is dominated by a weak [0001] maxima aligned in the direction of the applied stress and girdles in the orthogonal directions (e.g. $[10\bar{1}0]$, $[2\bar{1}\bar{1}0]$). It is consistent with slip of dislocations along the basal plane. The intra-grain misorientation angles (Figures 8e, 8h) are generally low but in many grains definitively non-zero, implying there is a low dislocation density in the samples. The highest of the intra-grain misorientation angles could possibly be due to errors in grain segmentation. It is possible that any dislocations annealed out of the samples in the time taken for the experiments to cool down after the temperature was quenched. This though seems unlikely because the last measurements in both experiments were at $< 200\,^{\circ}\mathrm{C}$ when quenched and cooling to $< 50\,^{\circ}\mathrm{C}$ takes less than a minute.

The distribution of grain-grain misorientation angles is very similar for the two recovered samples and very different from that of the initial wire (Figure 9b). The distributions are similar to those expected for a random powder with the same Orientation Distribution Function (ODF) as the samples except at low angles, where there are more low-angle grain boundaries between 5 and 10° than expected. The high number of small grain-boundaries is likely due to the low grain segmentation threshold which has divided the more highly distorted grains into multiple separate units. There is no large difference between the observed grain-misorientation distribution and a random distribution drawn from the samples's LPO that would be indicative of a strong recrystallistion relationship between the parent and child grains [*Wheeler et al.*, 2001].

The angle between twins in zinc is almost 90°. The drawn wire sample has a significant number of grain-boundaries between 80 and 90° which are likely to be due to twin-boundaries. In the recovered samples though, high angle grain-boundaries occur with approximately the frequency expected from the ODF and only a few twin boundaries can be present in the samples.

The similarity in the overall fabric of the recovered samples coupled with the significant grain-size reduction indicates that the recovered fabric has developed during the experiment and is likely controlled by the experimental conditions. The similarity of the grain-size between the recovered samples, the low dislocation density and disequilibrium grain shapes implies rapid recrystallisation of the samples during the experiment. This is consistent with the rapid growth and disappearance of peaks in the zinc diffraction observations. Zinc is highly susceptible to grain-growth and at elevated temperatures would ordinarily grain-grow very quickly, producing a very large grain-size (e.g. the drawn wire).

Diffusion is not insignificant on the time scale of the experiment. The platinum marker foils adjacent to the zinc noticeably thicken and blur into the zinc sample during the experiments while the thickness of the foils away from the zinc remains constant. The foils double their apparent thickness over the 12-24 hours of the experiments. It is not possible to determine from the recovered samples what role, if any, diffusion plays in the anelastic dissipation mechanism.

Therefore, the dissipation during the sinusoidal deformation is caused by dynamic recrystalistion with or without a significant contribution from grain-boundary sliding and diffusion. This prevents the growth of large crystals and instead establishes a quasi-equilibrium grain-size which is constantly reforming. The establishment of a steady-state grain-size and fabric here is similar to the steady-state foliation that occurs in natural rocks [*Means*, 1981] and implies an overall balance between the grain-boundary and internal energy of the grains. What the particular driving forces are (e.g. high dislocation density, grain boundary curvature) and how they are balanced we are unable to tell from the present analysis.

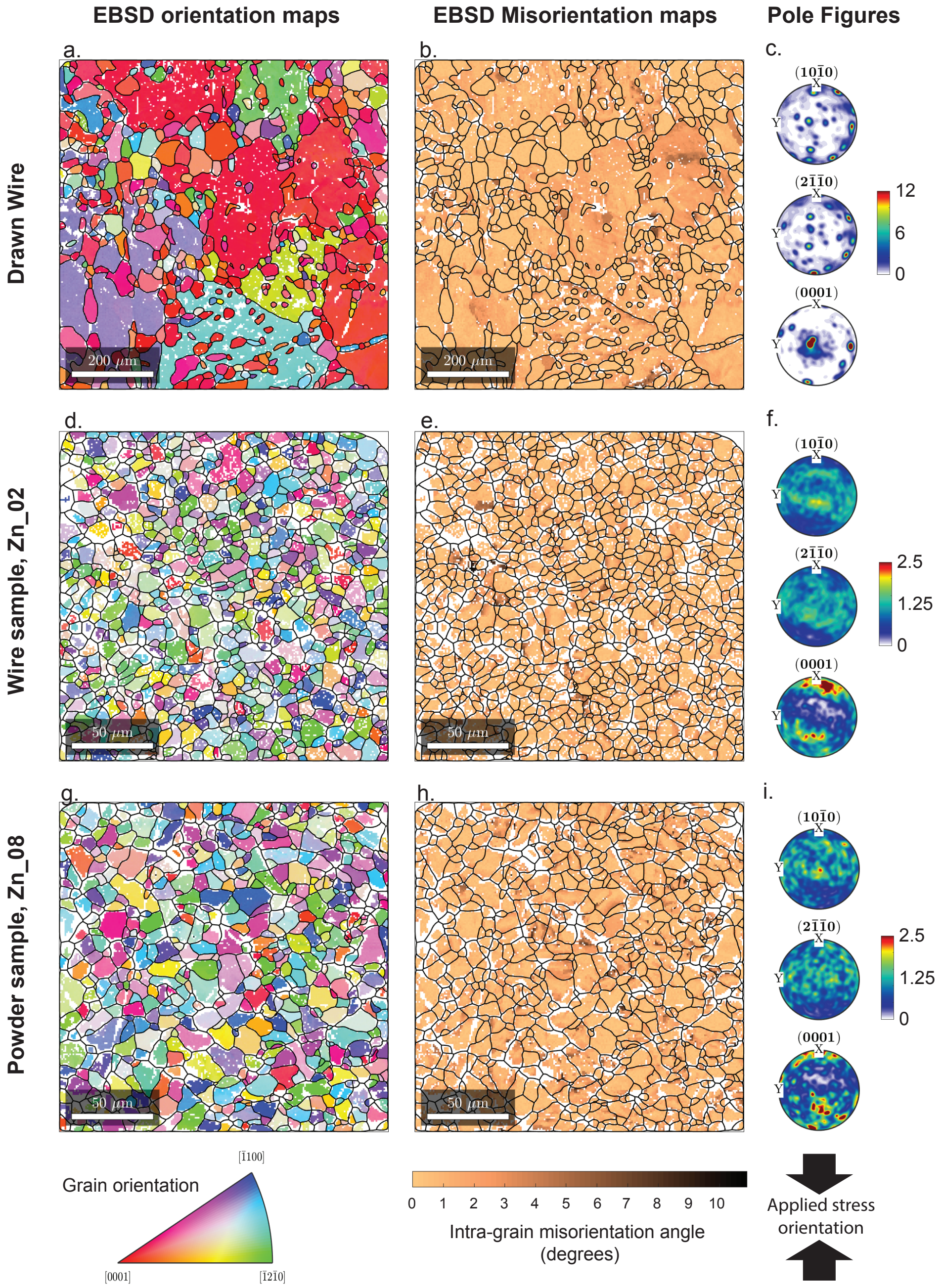

Figure 8. EBSD analysis of the samples. Top row (a, b, c): drawn wire before experiment, middle (d, e, f): wire after experiment (Zn_02) and bottom row (g, h i): powder after experiment. In each row the fist column (a, d, g) is an EBSD maps coloured by Euler angle, the middle column (b, e, h) is the intra-grain misorientation and the final column are total area, lower hemisphere, antipodal pole figures. The drawing direction (a, b, c) and applied sinusoidal stress and strain (d – i) is vertically in the figure. The corresponding colour scales are at the bottom of the figure. Note the difference in spatial and pole figure scales between the drawn wire and the recovered samples.

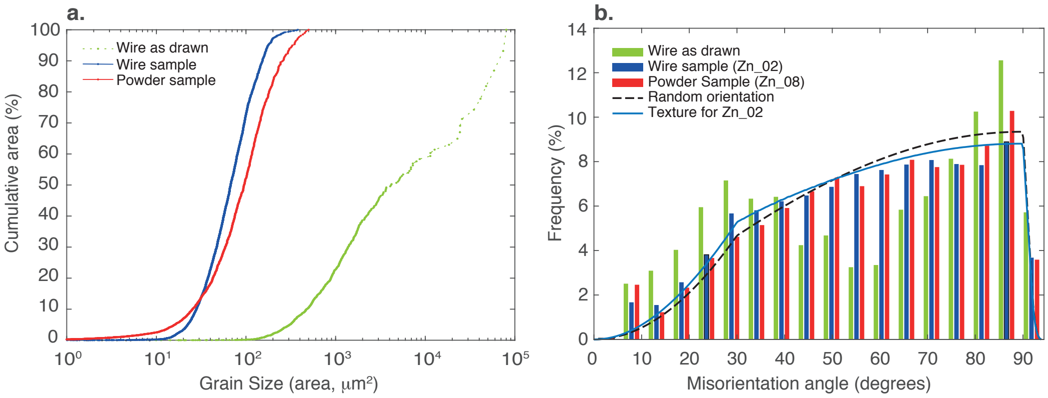

Figure 9. Grain size and grain-grain misorientation distributions. (a) Cumulative grain size distributions for the original wire and the recovered experimental samples respectively. (b) Misorientation of adjacent grains for wire and two recovered samples. The black dashed and solid blue lines are the expected misorientation distributions derived for a random distribution and the LPO measured in the wire sample (Figure 8f).

6 Discussion

One of the most commonly considered parameters for attenuation at seismic frequencies is α, which is the power-law exponent that defines the change in attenuation with frequency at a given temperature [e.g., Eqs. 1 and 88 in *Jackson et al.*, 2000; *Brennan and Smylie*, 1981, respectively]:

$$Q^{-1}(\omega) = Q_0^{-1}\omega^{\alpha} \tag{11}$$

This approximation works well if there is a broad range of frequencies over which the dissipation occurs, rather than just a single frequency as in the Burgers model used here. Previous studies [e.g. *Jackson et al.*, 2000] found the above equation was a good approximation to the data. Due to both the spread of the data and the non-linear dependence of Q^{-1} with frequency, the applicability of this power-law relationship to the data in this study is more dubious. Nevertheless, values of α were determined by an unweighted Least Squares fit of the Q^{-1} values at each temperature (Figure 10). The values of α range between 0.1 and 0.8 with a median of ~0.2 and they show no definitive temperature dependence. The values for the powder sample are slightly larger than those of the wire.

To complement the directly calculated values, an effective value of α was also derived from the Burgers' model. Two estimates were calculated; the first using only the

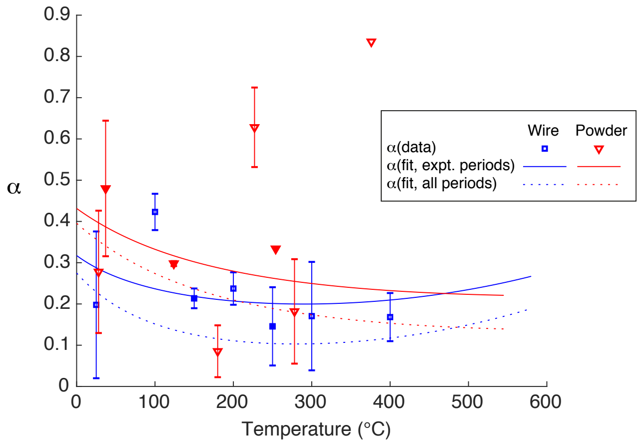

Figure 10. Change in α with temperature. Values of α are calculated directly from experimental data, the solid lines are from the Burgers model at the periods of the data and the dashed lines are from the Burgers models for all periods within the data range. Blue squares and lines denote the wire and the red triangles and lines are for powder. The open symbols are the data collected before the maximum temperature of the experiment and the filled symbols after.

periods present in the experimental data and the second using the continuum of periods filling the range of the experimental data. The α values calculated from the Burgers model with only the experimental frequencies show good correspondence with the experimental values and at the melting temperature of zinc in the experiments both have values of ~0.3. Calculating α from the Burgers model using all possible periods within the frequency range reduces the values to ~0.2 at the melting temperature of zinc. The values of α here are very similar to the values in iron from *Jackson et al.* [2000].

The experiments here show significant softening in zinc at seismic frequencies which is expected to reduce the sound velocity through the material. Calculation of v_p and v_s in an isotropic medium requires knowledge of both the shear modulus and Young's modulus (or two pieces of equivalent information) but here we have only measured the Young's modulus. Although formally, in an anelastic system the bulk modulus (K) is also anelastic [*Anderson*, 1989; *Nowick and Berry*, 1972] we assume here the effective bulk modulus is unaffected by the dissipation mechanism. This is reasonable because recrystallisation, grain-boundary sliding or the presence of dislocations should not affect the compressibility. Assuming a bulk modulus with the same anelastic dissipation as the Young's modulus compounds the softening making it much more significant and increasing the reductions in v_p and v_s. The elastic bulk modulus (K) gives the second piece of information with which to calculate v_p and v_s from the following relations:

$$v_p(\omega) = \sqrt{\frac{3K[3K + E(\omega)]}{\rho[9K - E(\omega)]}} \tag{12a}$$

$$v_s(\omega) = \sqrt{-\frac{3KE(\omega)}{\rho[E(\omega) - 9K]}} \tag{12b}$$

where ρ is the density. The bulk modulus was calculated in a the same way as the Young's modulae, using the elastic stiffnesses of zinc at the mean pressure of each experiment. The density was calculated using a reference density of $7.12\,\mathrm{g\,cm^{-3}}$, the calculated bulk modulus and the thermal expansion coefficients of *Nuss et al.* [2010].

The sound speed at finite frequency, calculated from the Burger's model finite frequency Young's modulus of zinc and Equation 12 is plotted in Figure 11. Close to melting, both Burgers models predict similar reductions in sound speed as a function of frequency. For a 30 s period the reductions in v_p are 0.05 and $0.11\,\mathrm{km\,s^{-1}}$ for the wire and powder samples respectively; the corresponding reductions in v_s are 0.11 and $0.17\,\mathrm{km\,s^{-1}}$. These correspond to percentage reductions in sound velocity of 1.4 and 2.6 % for v_p and 7.8 and 8.5 % for v_s. The absolute reduction in $v_s(\omega)$ is between 1.5 and two times greater than the reduction in $v_p(\omega)$, which in consistent with the inner-core in which $v_s(\omega)$ is reduced more than $v_p(\omega)$ relative to pure Fe at infinite frequency. The frequency dependent Poisson's ratio increases with period and for a 30 s period is predicted to be ~ 0.1 greater than the elastic values. The temperature dependence of these values is small compared to the change in velocity with temperature and there is no evidence from our data of additional deviations close to the melting temperature.

The value of $Q(\omega)$ measured in these experiments is 10-20 times greater than that reported for the inner-core, possibly because the experiments are not in the linear regime and significantly over-driven compared to the stress imparted in seismic waves passing through the inner-core. The strains though were the smallest that could be observed while performing the experiments. Outside of the linear anelastic regime, large stresses decrease the values of $E(\omega)$ and increase $Q^{-1}(\omega)$ [e.g. *Li and Weidner*, 2007] . The large stresses will enhance creep in the samples, thus providing a lower bound for $E(\omega)$ and an upper bound for $Q^{-1}(\omega)$. Therefore, the predicted reductions in sound velocity should be regarded as an upper bound and anelastic reduction of inner core seismic velocity is likely to be smaller than determined here.

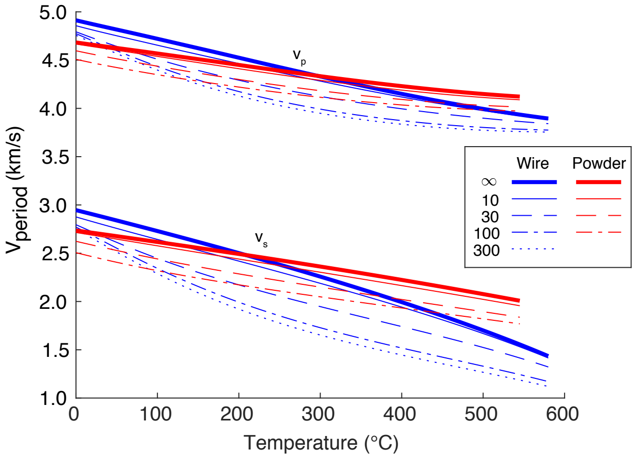

Figure 11. Sound velocity as a function of temperature and period for both the wire and the powder experiments, calculated from the Burgers models and Equation 11. Blue lines denote the wire sample and the red lines the powder sample.

Nevertheless, the correspondence of deformation properties in *hcp* metals can be used to make first order inferences about the anelasticity of the inner core. The innre core is very close to the melting temperature of its alloy and at high temperature iron, like zinc, undergoes rapid recrystallisaion [*Anzellini et al.*, 2013]. Therefore it is likely that the inner core is undergoing rapid recrystallisation, which we have shown here gives rise to, or related to, the dissipation. In the inner core, there will be some reduction of inner core seismic velocity because the core has a finite value of Q^{-1}. Any reduction of the inner core seismic wave speed by anelastic effects will result in an underestimation of the inner core's elastic moduli (K and μ). The estimated difference between the elastic properties of pure iron and that of the inner core are therefore overestimated. Thus comparison of seismic wave speed with experimental or computed material properties will tend to over estimate the light element budget of the inner core and needs to be considered in future studies.

7 Conclusions

The high-pressure response of zinc wire and powder samples to sinusoidal stress at seismic frequencies and up $T/T_M \sim 0.8$ have been measured and shows that the *hcp*-metal zinc has significant anelastic dissipation at seismic frequencies. The Burgers model used to fit the data successfully reproduces the features of the zinc anelasticity data produced in this study. The elastic (E_M) components of the model show a good correspondence to previous studies (Figure 7). The activation energy for creep (η_M) is much lower than previous studies have found; the values of E_V and η_V are less well constrained and do not correspond simply to a single physical process. It is therefore probable that the Burgers model is too simplistic to properly describe the dissipate processes active in the sample but there is not sufficient data to warrant the use of more complex models. Nevertheless, the experiments here show that significant anelastic softening occurs at high pressure and temperature in zinc and by extension *hcp* metals.

The recovered samples have very similar grain-size and LPO (Figures 8 and 9a) despite the initial grain-size and fabric being very different. The small amplitude deformation during the experiment appears to have prevented the growth of large grains and the grain-size is therefore in a steady-state fabric, analogous to the steady-state foliation of *Means* [1981]. The grains are not equant equilibrium shapes and have very few dislocations and sub-grain boundaries It seems likely that the anelastic dissipation is caused by dynamic recrystallisation (with or without contributions from grain-boundary sliding and diffusion), which also prevented measurement of attenuation anisotropy in the samples. We therefore conclude that the softening is caused by the same mechanism in both experiments and that the differences between the experiments are caused by imperfections in the experimental geometry. To the best of our knowledge this is the first observation of a dynamic recrystallisation as an anelastic dissipation mechanism.

Associated with the dissipation is a significant drop in the effective Youngs modulus with increasing period and an associated reduction in sound speed. Calculating frequency dependent wave speed shows that the anelastic dissipation reduces v_s 2 and 3 times more than it does v_p. This is consistent with observations of the inner core, where the reduction in v_s is much larger than that in v_p. Accounting for anelastic reductions in sound velocity will increase the elastic modulae and sound velocities of the inner-core alloy closer to those of pure iron. Anelastic effects may therefore imply that the light element budget of the inner core is less than previously considered.

The significant dissipation observed in these experiments occurs even in the absence of a fluid phase or significant impurities. Thus anelasticity must be accounted for when interpreting the inner-core's structure and seismic velocity.

A Temperature Calibration

Thermal gradients in small multi-anvil cells are potentially significant and increase with temperature and distance from the centre of the furnace [*Liebermann and Wang*, 1992; *Hernlund et al.*, 2006]. The corundum standard which was used to measure the pressure and determine the standard's Youngs modulus was not in the centre of the furnace or immediately adjacent to the thermocouple. A temperature difference between the thermocouple and the corundum standard could result in a systematic underestimation of the Young's modulus of corundum, an error which would propagate into the analysis of anelastic dissipation.

To determine if a significant temperature gradient or difference existed in the experimental cell experiment Zn_06 was performed in which the temperature was ramped until the zinc melted. The temperature at which melting occurs is an independent, absolute, reference of the temperature in the experiment. The cell in this experiment was the same as the other experiments and the sample was zinc wire. At the same load as before (270 kN), the experiment was heated from 150 °C to ~570 °C over a period of 3 hrs 35 mins, by which point the zinc had melted. During heating X-radiographs were collected at a rate of 1.5 s/frame. Diffraction patterns were collected intermittently during the temperature ramp.

The melting point of the zinc was determined from the radiographs; when the zinc melted a plume of platinum-rich material rose through the sample. Although the sample melted it did not make a ball of molten metal in the cell because convection stirred platinum into the sample. There is no eutectic depression of the melting point at the zinc-rich end of the Zn-Pt binary [*Moser*, 1991] and adding platinum to zinc increases the melting temperature and re-froze the sample. The thermocouple temperature was 544 °C when the zinc melted; the error in this measurement is negligible. From the zinc melting curve [$T_{M,0} = 419.5°\text{C}, \mathrm{d}T_M/\mathrm{d}P = 40\,\text{K/GPa}$; *Errandonea*, 2010] this temperature corresponds to 3.11 GPa.

During heating the pressure was measured by diffraction from the corundum at 27, 225, 289, 368 and 422 °C. Assuming the temperature in the corundum was the same as the thermocouple reported, the pressures were 3.83(48), 3.52(26), 3.50(15), 3.53(23) and 3.37(34) GPa. A linear fit of the pressure against temperature gives a reduction in pressure of $-1.04\,\text{MPa}\,\text{K}^{-1}$ and intercepts the melting curve at 550(13) °C and 3.26(33) GPa.

These estimates are within error of the observed melting conditions. Any differences in temperature between the thermocouple, zinc sample and corundum standard are therefore insignificant and no temperature correction is required.

B Maxwell Model

The Maxwell model (Figure 4a) along with the Voigt model (Figure 4b) are the two simplest models that contain intrinsic attenuation and thus frequency dependent behaviour. Integrating over the creep function of the Maxwell model gives [*Faul and Jackson*, 2015]:

$$J^*(\omega) = J_M(1 + 1/\mathrm{i}\omega\tau_M); \quad J_1 = J_M; \quad J_2 = J_M/\mathrm{i}\omega\tau_M; \quad Q = 1/\omega\tau_M \tag{B.1}$$

where the relaxation time is $\tau_M = \eta_M/k$ and η_M is the viscosity. Written in terms of the the independent properties of the spring constant (k) and viscosity (η):

$$J^*(\omega) = \frac{1}{k}\left(1 + \frac{1}{\mathrm{i}\omega\eta/k}\right); \quad J_1 = \frac{1}{k}; \quad J_2 = \frac{k}{\mathrm{i}\omega\eta}; \quad Q = \frac{1}{\omega\eta/k} \tag{B.2}$$

Equation B.2 shows that the Maxwell model's frequency dependence of Q is proportional to period and cannot contain any inflection points (i.e. $d^2Q(\omega)/d\omega^2 \neq 0$). The Voigt/Kelvin model has Q inversely proportional to period and is also without the possibility of inflection points.

C Andrade Model

The Andrade model (Figure 4c) is a phenomenological model derived from microcreep experiments and provides a good fit to the transient, pre-steady state, part of creep curves [*Sundberg and Cooper*, 2010; *Cooper*, 2002]. For the Andrade model [*Faul and Jackson*, 2015]:

$$J^*(\omega) = J_U + \beta\Gamma(1+n)(\mathrm{i}\omega)^{-n} - \mathrm{i}/\eta\omega. \tag{C.1}$$

Rearranging this to the same form as Equation 10 gives:

$$J_1(\omega) = J_U + \beta\Gamma(1+n)(\mathrm{i}\omega)^{-n}\cos(n\pi/2) \tag{C.2a}$$

$$J_2(\omega) = \beta\Gamma(1+n)(\mathrm{i}\omega)^{-n}\sin(n\pi/2) - \mathrm{i}/\eta\omega \tag{C.2b}$$

where $\Gamma(1+n)$ is the gamma function [*Gribb and Cooper*, 1998] and $J_U = 1/k_M$, β, n and η are the material properties of the different components of the model (Figure 4c). The parameters β and n describe the shape of the transient seen during creep experiments and under oscillatory stress provide damping over a wide range of frequencies. The value of *n* has been constrained experimentally to be approximately 1/3 [*Gribb and Cooper*, 1998]. Because dissipation occurs over a wide range of frequencies, the Andrade model has been argued to provide a physically consistent description of both the rheological and anelastic properties of peridotite [*Sundberg and Cooper*, 2010].

Acknowledgements

S.A.H. (NE/H016309, NE/L006898, NE/P017525), A.M.W (NE/K008803/1 and NE/M000044/1) and O.T.L (NE/J018945/1) thank the Natural Environment Research Council (NERC) for funding. Use of the National Synchrotron Light Source (NSLS), Brookhaven National Laboratory, was supported by the U.S. Department of Energy, Office of Science, Office of Basic Energy Sciences, under Contract No. DE-AC02-98CH10886. Use of the X17B2 beamline was supported by COMPRES, the Consortium for Materials Properties Research in Earth Sciences under NSF Cooperative Agreement EAR 10-43050 and by the Mineral Physics Institute, Stony Brook University.

The data collected in the course of this study is available from https://www.bgs.ac.uk/discoverymetadata/13607352.html

References

Alers, G., and J. Neighbours (1958), The elastic constants of zinc between 4.2° and 670 °K, *Journal of Physics and Chemistry of Solids*, *7*(1), 58–64, doi:10.1016/0022-3697(58)90180-x.

Anderson, D. L. (1989), *Theory of the Earth*, Boston: Blackwell Scientific Publications.

Anderson, D. L., and J. B. Minster (1979), The frequency dependence of Q in the Earth and implications for mantle rheology and chandler wobble, *Geophysical Journal International*, *58*(2), 431–440, doi:10.1111/j.1365-246x.1979.tb01033.x.

Aning, A., T. Suzuki, and M. Wuttig (1982), Nonlinear anelasticity of magnesium, *Journal of Applied Physics*, *53*(10), 6797–6808, doi:10.1063/1.330068.

Antonangeli, D., J. Siebert, J. Badro, D. L. Farber, G. Fiquet, G. Morard, and F. J. Ryerson (2010), Composition of the Earth’s inner core from high-pressure sound velocity measurements in Fe-Ni-Si alloys, *Earth and Planetary Science Letters*, *295*(1-2), 292–296, doi:10.1016/j.epsl.2010.04.018.

Antonangeli, D., G. Morard, L. Paolasini, G. Garbarino, C. A. Murphy, E. Edmund, F. Decremps, G. Fiquet, A. Bosak, M. Mezouar, and Y. Fei (2018), Sound velocities and density measurements of solid hcp-Fe and hcp-Fe-Si (9 wt.%) alloy at high pressure: Constraints on the Si abundance in the Earth's inner core, *Earth and Plane-*

tary Science Letters, *482*, 446–453, doi:10.1016/j.epsl.2017.11.043.

Anzellini, S., A. Dewaele, M. Mezouar, P. Loubeyre, and G. Morard (2013), Melting of iron at Earth's inner core boundary based on fast x-ray diffraction, *Science*, *340*(6131), 464–466, doi:10.1126/science.1233514.

Aubert, J., H. Amit, G. Hulot, and P. Olson (2008), Thermochemical flows couple the Earth's inner core growth to mantle heterogeneity, *Nature*, *454*(7205), 758–761, doi:10.1038/nature07109.

Bachmann, F., R. Hielscher, and H. Schaeben (2010), Texture analysis with MTEX–free and open source software toolbox, *Solid State Phenomena*, *160*, 63–68, doi:10.4028/www.scientific.net/SSP.160.63.

Bachmann, F., R. Hielscher, and H. Schaeben (2011), Grain detection from 2d and 3d EBSD data – specification of the MTEX algorithm, *Ultramicroscopy*, *111*(12), 1720–1733, doi:10.1016/j.ultramic.2011.08.002.

Bazhanova, Z. G., V. V. Roizen, and A. R. Oganov (2017), High-pressure behavior of the Fe-S system and composition of the Earth's inner core, *Physics-Uspekhi*, *60*(10), 1025–1032, doi:10.3367/ufne.2017.03.038079.

Belonoshko, A. B., J. Fu, T. Bryk, S. I. Simak, and M. Mattesini (2019), Low viscosity of the Earth's inner core, *Nature Communications*, *10*(1), doi:10.1038/s41467-019-10346-2.

Brennan, B. J., and D. E. Smylie (1981), Linear viscoelasticity and dispersion in seismic wave propagation, *Reviews of Geophysics*, *19*(2), 233, doi:10.1029/rg019i002p00233.

Cao, A., and B. Romanowicz (2004), Hemispherical transition of seismic attenuation at the top of the Earth's inner core, *Earth and Planetary Science Letters*, *228*(3-4), 243–253, doi:10.1016/j.epsl.2004.09.032.

Caracas, R. (2015), The influence of hydrogen on the seismic properties of solid iron, *Geophysical Research Letters*, *42*(10), 3780–3785, doi:10.1002/2015gl063478.

Chabildas, L. C., and H. M. Gilder (1972), Thermal coefficient of expansion of an activated vacancy in zinc from high-pressure self-diffusion experiments, *Physical Review B*, *5*(6), 2135–2144, doi:10.1103/physrevb.5.2135.

Cooper, R. F. (2002), Seismic wave attenuation: Energy dissipation in viscoelastic crystalline solids, *Reviews in Mineralogy and Geochemistry*, *51*(1), 253–290, doi:10.2138/gsrmg.51.1.253.

Cottrell, A. H., and V. Aytekin (1947), Andrade's creep law and the flow of zinc crystals, *Nature*, *160*, 328–329.

Deuss, A. (2014), Heterogeneity and anisotropy of Earth's inner core, *Annual Review of Earth and Planetary Sciences*, *42*(1), 103–126, doi:10.1146/annurev-Earth-060313-054658.

Dobson, D. P., S. A. Hunt, L. Li, and D. J. Weidner (2008), Measurement of thermal diffusivity at high pressures and temperatures using synchrotron radiography., *Mineralogical Magazine*, *72*(2), 653 – 658, doi:10.1180/minmag.2008.072.2.653.

Dobson, D. P., S. A. Hunt, R. McCormack, O. T. Lord, D. J. Weidner, L. Li, and A. M. Walker (2010), Thermal diffusivity of MORB-composition rocks to 15 GPa: implications for triggering of deep seismicity, *High Pressure Research*, *30*(3), 406 – 414, doi:10.1080/08957959.2010.516827.

Dobson, D. P., R. McCormack, S. A. Hunt, M. W. Ammann, D. Weidner, L. Li, and L. Wang (2012), The relative strength of perovskite and post-perovskite $NaCoF_3$, *Mineralogical Magazine*, *76*(4), 925 – 932, doi: 10.1180/minmag.2012.076.4.09.

Doornbos, D. J. (1974), The anelasticity of the inner core, *Geophysical Journal International*, *38*(2), 397–415, doi: 10.1111/j.1365-246x.1974.tb04131.x.

Durham, W. B., D. J. Weidner, S. I. Karato, and Y. B. Wang (2002), New developments in deformation experiments at high pressure, in *Plastic Deformation of Minerals and Rocks*, *Reviews in Mineralogy & Geochemistry*, vol. 51, edited by S. Karato and H. Wenk, pp. 21–49, Mineral. Soc. Am., doi:10.2138/gsrmg.51.1.21.

Errandonea, D. (2010), The melting curve of ten metals up to 12 GPa and 1600 K, *Journal of Applied Physics*, *108*(3), 033,517, doi:10.1063/1.3468149.

Faul, U., and I. Jackson (2015), Transient creep and strain energy dissipation: An experimental perspective, *Annual Review of Earth and Planetary Sciences*, *43*(1), 541–569, doi:10.1146/annurev-Earth-060313-054732.

Fearn, D. R., D. E. Loper, and P. H. Roberts (1981), Structure of the Earth's inner core, *Nature*, *292*(5820), 232–233, doi:10.1038/292232a0.

Fei, Y. (1995), Thermal expansion, in *AGU Reference Shelf*, pp. 29–44, American Geophysical Union, doi: 10.1029/rf002p0029.

Fei, Y., C. Murphy, Y. Shibazaki, A. Shahar, and H. Huang (2016), Thermal equation of state of hcp-iron: Constraint on the density deficit of Earth's solid inner core, *Geophysical Research Letters*, *43*(13), 6837–6843, doi: 10.1002/2016gl069456.

Fiquet, G. (2001), Sound velocities in iron to 110 Gigapascals, *Science*, *291*(5503), 468–471, doi: 10.1126/science.291.5503.468.

Fischer, R. A., and A. J. Campbell (2015), The axial ratio of hcp Fe and Fe–Ni–Si alloys to the conditions of Earth's inner core, *American Mineralogist*, *100*, 2718–2724, doi:10.2138/am-2015-5191.

Frost, H., and M. Ashby (1982), *Deformation mechanism maps: the plasticity and creep of metals and ceramics*, Pergamon Press, Oxford, UK.

Gallier, J. H. (2000), *Curves and surfaces in geometric modeling: theory and algorithms*, Morgan Kaufmann series in computer graphics and geometric modeling, Morgan Kaufmann Publishers.

Gieske, J. H., and G. R. Barsch (1968), Pressure dependence of the elastic constants of single crystalline aluminum oxide, *Physica Status Solidi (b)*, *29*(1), 121–131, doi:10.1002/pssb.19680290113.

Goto, T., O. L. Anderson, I. Ohno, and S. Yamamoto (1989), Elastic constants of corundum up to 1825 K, *Journal of Geophysical Research*, *94*(B6), 7588, doi:10.1029/jb094ib06p07588.

Gribb, T. T., and R. F. Cooper (1998), Low-frequency shear attenuation in polycrystalline olivine: Grain boundary diffusion and the physical significance of the Andrade model for viscoelastic rheology, *Journal of Geophysical*

Research: Solid Earth, *103*(B11), 27,267–27,279, doi:10.1029/98jb02786.

Hernlund, J., K. Leinedweber, D. Locke, and J. A. Tyburzy (2006), A numerical model for steady-state temperature distributions in solid-medium high-pressure cell assemblies, *American Mineralogist*, *91*(2-3), 295–305, doi: 10.2138/am.2006.1938.

Hunt, S. A., A. M. Walker, R. McCormack, D. P. Dobson, A. S. Wills, and L. Li (2011), The effect of pressure on thermal diffusivity in pyroxenes, *Mineralogical Magazine*, *75*(5), 2597–2610, doi: 10.1180/minmag.2011.075.5.2597.

Hunt, S. A., D. R. Davies, A. M. Walker, R. J. McCormack, A. S. Wills, D. P. Dobson, and L. Li (2012), On the increase in thermal diffusivity caused by the perovskite to post-perovskite phase transition and its implications for mantle dynamics, *Earth and Planetary Science Letters*, *319 - 320*, 96 – 103, doi:10.1016/j.epsl.2011.12.009.

Irving, J. C., and A. Deuss (2011), Stratified anisotropic structure at the top of Earth's inner core: A normal mode study, *Physics of the Earth and Planetary Interiors*, *186*(1-2), 59–69, doi:10.1016/j.pepi.2011.03.003.

Jackson, I. (2015), Properties of rocks and minerals: Physical origins of anelasticity and attenuation in rock, in *Treatise on Geophysics*, pp. 539–571, Elsevier, doi:10.1016/b978-0-444-53802-4.00045-2.

Jackson, I., J. D. F. Gerald, and H. Kokkonen (2000), High-temperature viscoelastic relaxation in iron and its implications for the shear modulus and attenuation of the Earth's inner core, *Journal of Geophysical Research: Solid Earth*, *105*(B10), 23,605–23,634, doi:10.1029/2000jb900131.

Ledbetter, H. M. (1977), Elastic properties of zinc: A compilation and a review, *Journal of Physical and Chemical Reference Data*, *6*(4), 1181–1203, doi:10.1063/1.555564.

Li, L., and D. J. Weidner (2007), Energy dissipation of materials at high pressure and high temperature, *Review of Scientific Instruments*, *78*(5), 053,902, doi:10.1063/1.2735587.

Li, L., P. Raterron, D. J. Weidner, and J. Chen (2003), Olivine flow mechanisms at 8 GPa, *Physics of The Earth and Planetary Interiors*, *138*, 113 – 129, doi:10.1016/S0031-9201(03)00065-7.

Li, X., and V. F. Cormier (2002), Frequency-dependent seismic attenuation in the inner core, 1. a viscoelastic interpretation, *Journal of Geophysical Research: Solid Earth*, *107*(B12), ESE 13–1–ESE 13–20, doi: 10.1029/2002jb001795.

Li, Y., L. Vočadlo, and J. P. Brodholt (2018), The elastic properties of hcp-Fe alloys under the conditions of the Earth's inner core, *Earth and Planetary Science Letters*, *493*, 118–127, doi:10.1016/j.epsl.2018.04.013.

Liebermann, R. C., and Y. Wang (1992), Characterization of sample environment in a uniaxial split-sphere apparatus, in *High-Pressure Research: Application to Earth and Planetary Sciences*, edited by Y. Syono and M. H. Manghnani, pp. 19–31, American Geophysical Union, doi:10.1029/gm067p0019.

Lloyd, G. E. (1987), Atomic number and crystallographic contrast images with the SEM: a review of backscattered electron techniques, *Mineralogical Magazine*, *51*, 3–19, doi:10.1180/minmag.1987.051.359.02.

Lythgoe, K., A. Deuss, J. Rudge, and J. Neufeld (2014), Earth's inner core: Innermost inner core or hemispherical variations?, *Earth and Planetary Science Letters*, *385*, 181–189, doi:10.1016/j.epsl.2013.10.049.

Mäkinen, A. M., A. Deuss, and S. A. T. Redfern (2014), Anisotropy of Earth's inner core intrinsic attenuation from seismic normal mode models, *Earth and Planetary Science Letters*, *404*, 354–364, doi:10.1016/j.epsl.2014.08.009.

Mao, Z., J.-F. Lin, J. Liu, A. Alatas, L. Gao, J. Zhao, and H.-K. Mao (2012), Sound velocities of Fe and Fe-Si alloy in the Earth's core, *Proceedings of the National Academy of Sciences*, *109*(26), 10,239–10,244, doi:10.1073/pnas.1207086109.

Means, W. D. (1981), The concept of steady-state foliation, *Tectonophysics*, *78*(1), 179 – 199, doi:10.1016/0040-1951(81)90013-5.

Merkel, S., H.-R. Wenk, P. Gillet, H. kwang Mao, and R. J. Hemley (2004), Deformation of polycrystalline iron up to 30 GPa and 1000 K, *Physics of the Earth and Planetary Interiors*, *145*(1-4), 239–251, doi:10.1016/j.pepi.2004.04.001.

Miyagi, L., M. Kunz, J. Knight, J. Nasiatka, M. Voltolini, and H.-R. Wenk (2008), In situ phase transformation and deformation of iron at high pressure and temperature, *Journal of Applied Physics*, *104*(10), 103,510, doi:10.1063/1.3008035.

Morelli, A., A. M. Dziewonski, and J. H. Woodhouse (1986), Anisotropy of the inner core inferred from PKIKP travel times, *Geophysical Research Letters*, *13*(13), 1545–1548, doi:10.1029/gl013i013p01545.

Moser, Z. (1991), The Pt-Zn (platinum-zinc) system, *Journal of Phase Equilibria*, *12*, 439–443, doi:10.1007/BF02645964.

Murthy, G. S., and D. H. Sastry (1982), Impression creep of zinc and the rate-controlling dislocation mechanism of plastic flow at high temperatures, *physica status solidi (a)*, *70*(1), 63–71, doi:10.1002/pssa.2210700110.

Niu, F., and L. Wen (2001), Hemispherical variations in seismic velocity at the top of the Earth's inner core, *Nature*, *410*(6832), 1081–1084, doi:10.1038/35074073.

Nowick, A. S., and B. S. Berry (1972), *Anelastic Relaxation in Crystalline Solids*, Academic Press.

Nuss, J., U. Wedig, A. Kirfel, and M. Jansen (2010), The structural anomaly of zinc: Evolution of lattice constants and parameters of thermal motion in the temperature range of 40 to 500 K, *Zeitschrift fÃijr anorganische und allgemeine Chemie*, *636*(2), 309–313, doi:10.1002/zaac.200900460.

Orman, J. A. V. (2004), On the viscosity and creep mechanism of Earth's inner core, *Geophysical Research Letters*, *31*(20), doi:10.1029/2004gl021209.

Pejić, T., R. Hawkins, M. Sambridge, and H. Tkalčić (2019), Transdimensional bayesian attenuation tomography of the upper inner core, *Journal of Geophysical Research: Solid Earth*, *124*(2), 1929–1943, doi:10.1029/2018jb016400.

Pratt, W. K. (1991), *Digital Image Processing*, pp. 171–186, Wiley.

Prescher, C., L. Dubrovinsky, E. Bykova, I. Kupenko, K. Glazyrin, A. Kantor, C. McCammon, M. Mookherjee, Y. Nakajima, N. Miyajima, R. Sinmyo, V. Cerantola, N. Dubrovinskaia, V. Prakapenka, R. RÃijffer, A. Chumakov, and M. Hanfland (2015), High poisson's ratio of Earth's inner core explained by carbon alloying, *Nature Geoscience*, *8*(3), 220–223, doi:10.1038/ngeo2370.

Roberts, J. M., and N. Brown (1962), Low ferquency internal friction in zinc single crystals, *Acta Metalurgica*, *10*, 430 – 441.

Romanowicz, B., and B. Mitchell (2015), Deep Earth structure: Q of the Earth from crust to core, in *Treatise on Geophysics*, pp. 789–827, Elsevier, doi:10.1016/b978-0-444-53802-4.00021-x.

Sakamaki, T., E. Ohtani, H. Fukui, S. Kamada, S. Takahashi, T. Sakairi, A. Takahata, T. Sakai, S. Tsutsui, D. Ishikawa, R. Shiraishi, Y. Seto, T. Tsuchiya, and A. Q. R. Baron (2016), Constraints on Earth's inner core composition inferred from measurements of the sound velocity of hcp-iron in extreme conditions, *Science Advances*, *2*(2), e1500,802, doi:10.1126/sciadv.1500802.

Shearer, P. M. (1994), Constraints on inner core anisotropy from PKP(DF) travel times, *Journal of Geophysical Research: Solid Earth*, *99*(B10), 19,647–19,659, doi:10.1029/94jb01470.

Singh, S. C. (2000), On the presence of liquid in Earth's inner core, *Science*, *287*(5462), 2471–2474, doi:10.1126/science.287.5462.2471.

Srinivasan, R., and R. R. Rao (1971), Anharmonic properties of the hexagonal metals, magnesium, zinc and beryllium – i. lattice dynamics and third order elastic constants, *Journal of Physics and Chemistry of Solids*, *32*(8), 1769–1788, doi:10.1016/s0022-3697(71)80143-9.

Stein, S., and M. Wysession (2013), *An Introduction to Seismology, Earthquakes, and Earth Structure*, John Wiley & Sons.

Suda, N., and Y. Fukao (1990), Structure of the inner core inferred from observations of seismic core modes, *Geophysical Journal International*, *103*(2), 403–413, doi:10.1111/j.1365-246x.1990.tb01779.x.

Sumita, I., and M. Bergman (2015), Inner core dynamics, in *Treatise on Geophysics*, pp. 297–316, Elsevier, doi:10.1016/b978-0-444-53802-4.00143-3.

Sundberg, M., and R. F. Cooper (2010), A composite viscoelastic model for incorporating grain boundary sliding and transient diffusion creep: correlating creep and attenuation responses for materials with a fine grain size, *Philosophical Magazine*, *90*(20), 2817–2840, doi:10.1080/14786431003746656.

Tagawa, S., K. Ohta, K. Hirose, C. Kato, and Y. Ohishi (2016), Compression of Fe-Si-H alloys to core pressures, *Geophysical Research Letters*, *43*(8), 3686–3692, doi:10.1002/2016gl068848.

Takahashi, S. (1952), Anelasticity of zinc, *Journal of Applied Physics*, *23*(8), 866–868, doi:10.1063/1.1702321.

Tateno, S., K. Hirose, Y. Ohishi, and Y. Tatsumi (2010), The structure of iron in Earth's inner core, *Science*, *330*(6002), 359–361, doi:10.1126/science.1194662.

Tateno, S., K. Hirose, T. Komabayashi, H. Ozawa, and Y. Ohishi (2012), The structure of Fe-Ni alloy in Earth's inner core, *Geophysical Research Letters*, *39*(12), L052,103, doi:10.1029/2012GL052103.

Tateno, S., Y. Kuwayama, K. Hirose, and Y. Ohishi (2015), The structure of FeâĂŞSi alloy in Earth's inner core, *Earth and Planetary Science Letters*, *418*, 11–19, doi:10.1016/j.epsl.2015.02.008.

Tegart, W. J. M., and O. D. Sherby (1958), Activation energies for high temperature creep of polycrstalline zinc, *Philosophical Magazine*, *3*(35), 1287–1296, doi:10.1080/14786435808233311.

Thompson, D. O. (1955), Temperature dependent creep in zinc crystals, *Journal of Applied Physics*, *26*, 280–285, doi:10.1063/1.1721978.

Trucco, E., and A. Verri (1998), *Introductory Techniques for 3-D Computer Vision*, Prentice-Hall, Upper Saddle River, NJ, 343 pp.

Walker, A. M., and J. Wookey (2012), MSAT – a new toolkit for the analysis of elastic and seismic anisotropy, *Computers & Geosciences*, *49*, 81–90, doi:10.1016/j.cageo.2012.05.031.

Wang, Y., B. Durham, I. C. Getting, and D. J. Weidner (2003), The deformation-DIA: A new apparatus for high temperature triaxial deformation to pressures up to 15 GPa, *Review of Scientific Instruments*, *74*(6), 3002 – 3011, doi:10.1063/1.1570948.

Watanabe, T., S.-I. Kimura, and S. Karashima (1984), The effect of a grain boundary structural transformation on sliding in <1010>-tilt zinc bicrystals, *Philosophical Magazine A*, *49*(6), 845–864, doi:10.1080/01418618408236566.

Weidner, D. J., M. T. Vaughan, L. Wang, H. Long, L. Li, N. A. Dixon, and W. B. Durham (2010), Precise stress measurements with white synchrotron X-rays, *Review of Scientific Instruments*, *81*, 013,903, doi:10.1063/1.3263760.

Wheeler, J., D. Prior, Z. Jiang, R. Spiess, and P. Trimby (2001), The petrological significance of misorientations between grains, *Contributions to Mineralogy and Petrology*, *141*(1), 109–124, doi:10.1007/s004100000225.

Woodhouse, J. H., D. Giardini, and X.-D. Li (1986), Evidence for inner core anisotropy from free oscillations, *Geophysical Research Letters*, *13*(13), 1549–1552, doi:10.1029/gl013i013p01549.

Wuttig, M., A. Aning, and T. Suzuki (1981), Autooscillations in zinc, *Scripta Metallurgica*, *15*, 1237–1239, doi:10.1016/0036-9748(81)90306-9.

Yoo, M., S. Agnew, J. Morris, and K. Ho (2001), Non-basal slip systems in HCP metals and alloys: source mechanisms, *Materials Science and Engineering: A*, *319-321*, 87–92, doi:10.1016/s0921-5093(01)01027-9.

Yoo, M. H., and C. T. Wei (1967), Slip modes of hexagonal-close-packed metals, *Journal of Applied Physics*, *38*(11), 4317–4322, doi:10.1063/1.1709121.

Yu, W.-c., and L. Wen (2006), Inner core attenuation anisotropy, *Earth and Planetary Science Letters*, *245*(3-4), 581–594, doi:10.1016/j.epsl.2006.03.043.